PLANETARY SCIENCE

The dynamic atmospheric and aeolian environment of Jezero crater, Mars

Claire E. Newman[1]*, Ricardo Hueso[2]†, Mark T. Lemmon[3]†, Asier Munguira[2]‡, Álvaro Vicente-Retortillo[4]‡, Víctor Apestigue[5]§, Germán M. Martínez[6,7]§, Daniel Toledo[5]§, Rob Sullivan[8], Ken E. Herkenhoff[9], Manuel de la Torre Juárez[10], Mark I. Richardson[1], Alexander E. Stott[11], Naomi Murdoch[11], Agustín Sanchez-Lavega[2], Michael J. Wolff[3], Ignacio Arruego[5], Eduardo Sebastián[4], Sara Navarro[4], Javier Gómez-Elvira[4,5], Leslie Tamppari[10], Daniel Viúdez-Moreiras[4], Ari-Matti Harri[12], Maria Genzer[12], Maria Hieta[12], Ralph D. Lorenz[13], Pan Conrad[14], Felipe Gómez[4], Timothy H. McConnochie[3,15], David Mimoun[11], Christian Tate[8], Tanguy Bertrand[16], James F. Bell III[17], Justin N. Maki[10], Jose Antonio Rodriguez-Manfredi[4], Roger C. Wiens[18,19], Baptiste Chide[20], Sylvestre Maurice[20], Maria-Paz Zorzano[4], Luis Mora[4], Mariah M. Baker[21], Don Banfield[8,22], Jorge Pla-Garcia[3,4], Olivier Beyssac[23], Adrian Brown[24], Ben Clark[3], Alain Lepinette[4], Franck Montmessin[25], Erik Fischer[7], Priyaben Patel[26], Teresa del Río-Gaztelurrutia[2], Thierry Fouchet[16], Raymond Francis[10], Scott D. Guzewich[27]

Despite the importance of sand and dust to Mars geomorphology, weather, and exploration, the processes that move sand and that raise dust to maintain Mars' ubiquitous dust haze and to produce dust storms have not been well quantified in situ, with missions lacking either the necessary sensors or a sufficiently active aeolian environment. Perseverance rover's novel environmental sensors and Jezero crater's dusty environment remedy this. In Perseverance's first 216 sols, four convective vortices raised dust locally, while, on average, four passed the rover daily, over 25% of which were significantly dusty ("dust devils"). More rarely, dust lifting by nonvortex wind gusts was produced by daytime convection cells advected over the crater by strong regional daytime upslope winds, which also control aeolian surface features. One such event covered 10 times more area than the largest dust devil, suggesting that dust devils and wind gusts could raise equal amounts of dust under nonstorm conditions.

INTRODUCTION

Aeolian processes—the motion of surface sand and the lofting and redistribution of surface dust—are the primary causes of change to the Martian surface and atmosphere in the modern era (*1*, *2*). Large dust storms drastically alter atmospheric temperatures, densities, and circulation, presenting hazards to robotic and human missions, but atmospheric dust is also present year-round, impeding visibility and solar power (*3*, *4*). However, the mechanisms by which sand is moved and dust is lifted on Mars are not well quantified. This contributes to many outstanding questions, from what triggers the onset of global dust storms, which occur roughly three times per Mars decade, to what dust lifting processes are responsible for maintaining the background dust haze. Early studies, including analysis of Viking lander data, suggested that surface wind stresses on Mars might only rarely exceed the calculated threshold for moving sand-sized particles ($\gtrsim$40 μm in diameter) and thus would be even less likely to exceed the higher thresholds needed to raise smaller, more cohesive dust particles (*5*). However, this was inconsistent with observations of frequent dust storms and surface albedo changes attributed to widespread dust rearrangement (*6*, *2*). In the past decade, observations of active dunes from orbit and sand motion at the surface have also confirmed that saltation of sand particles occurs more widely over the Martian surface than suggested by earlier estimates (*7*, *8*).

A possible explanation is that Mars sand motion can be initiated by relatively short-lived strong wind gusts, which trigger substantial saltation downstream (*9*), and recent wind tunnel measurements support a lower saltation threshold than used previously (*10*). Once saltation first occurs, it can also continue more easily due to the sand saltating back to the surface and increasing the total stress, with this effect being far larger than on Earth (*11*). The same effect may also explain how dust is lifted despite the larger threshold stresses needed. However, in situ observations of dust lifting without apparent sand motion suggest that the presence of dust aggregates—larger clumps of dust particles with lower cohesion than individual grains—may be crucial (*12*) or that Mars' reduced gravity may modify the soil cohesion, making dust lifting easier (*13*). Last, convective vortices—termed "dust devils" when made visible by their dust content—may raise dust via a "suction effect"

[1]Aeolis Research, Chandler, AZ, USA. [2]Universidad del País Vasco UPV/EHU, Bilbao, Spain. [3]Space Science Institute, Boulder, CO, USA. [4]Centro de Astrobiologia, INTA, Madrid, Spain. [5]INTA, Madrid, Spain. [6]Lunar and Planetary Institute, USRA, Houston, TX, USA. [7]University of Michigan, Ann Arbor, MI, USA. [8]Cornell University, Ithaca, NY, USA. [9]USGS Astrogeology Science Center, Flagstaff, AZ, USA. [10]Jet Propulsion Laboratory–California Institute of Technology, Pasadena, CA, USA. [11]ISAE-SUPAERO, Université de Toulouse, Toulouse, France. [12]Finnish Meteorological Institute, Helsinki, Finland. [13]Johns Hopkins Applied Physics Lab, Laurel, MD, USA. [14]Carnegie Institution for Science, Washington, DC, USA. [15]University of Maryland, College Park, MD, USA. [16]LESIA, Observatoire de Paris, Meudon, France. [17]Arizona State University, Tempe, AZ, USA. [18]Los Alamos National Laboratory, Los Alamos, NM, USA. [19]Purdue University, West Lafayette, IN, USA. [20]IRAP-CNRS, Toulouse, France. [21]Smithsonian National Air and Space Museum, Washington, DC, USA. [22]NASA Ames, Mountain View, CA, USA. [23]IMPMC, CNRS-Sorbonne Université, Paris, France. [24]Plancius Research, Severna Park, MD, USA. [25]LATMOS, Guyancourt, France. [26]UCL, London, UK. [27]Goddard Space Flight Center, Greenbelt, MD, USA.
*Corresponding author. Email: claire@aeolisresearch.com
†These authors contributed equally to this work.
‡These authors contributed equally to this work.
§These authors contributed equally to this work.

associated with their low-pressure core, in addition to via the strong winds around them (*14*). Testing these ideas demands simultaneous measurements of aeolian activity and environmental variables, yet these are rare for Mars. Previous missions have generally either carried the necessary sensors or landed in an environment with substantial local sand motion and dust lifting but not both (*12*, *15*, *16*). Most recently, the Curiosity rover has observed substantial sand motion and many vortices and dust devils but could not measure winds easily (*8*, *17*, *18*), while the InSight lander has detected vortices but has imaged only minor surface changes and no dust devils (*19*, *20*).

By contrast, the Perseverance rover carries the most sophisticated atmospheric and dust sensors yet flown to Mars. The Mars Environmental Dynamics Analyzer (MEDA) (*21*) includes novel Radiation and Dust Sensors (RDS), which detect dust clouds and dust devils via changes to direct and scattered sunlight at 1-Hz frequency, simultaneous with MEDA measurements of pressure, temperature, wind, relative humidity, and also radiative fluxes from MEDA's Thermal InfraRed Sensor (TIRS). In combination, RDS and TIRS measurements of downward and upward shortwave radiation, respectively, provide information on albedo and also on albedo changes related to surface dust removal or deposition. Adding RDS and TIRS thus enables MEDA to track the passage of dusty phenomena around, past, and over the rover as a function of time over a large fraction of each sol and to relate this both to meteorological time series and surface changes, which would be impossible with imaging because of the huge amount of resources (cameras, power, and data volume) that would be required. Perseverance also carries the first microphones to operate on Mars, which provide information on turbulence, vortices, and wind activity (*22*), and high-resolution cameras including the Navigation cameras (Navcams) and Mastcam-Z, which may be used to image aeolian activity and features, such as dust devils and surface wind streaks (*23*, *24*). Most crucially, Jezero crater contains numerous aeolian surface features, imaged both from orbit (*25*, *26*) and since landing (see Results), and dozens of examples of aeolian activity have been observed over the first 216 sols of the mission, covering early spring through early summer [areocentric solar longitude (L_s) ~13° to 105°], as described in detail below. The Mars 2020 mission is thus a near-perfect combination of instrumentation and environment for studying atmospheric and aeolian connections.

RESULTS

Wind patterns and aeolian surface features are controlled by regional and local slopes

Aeolian processes are, by definition, driven by winds, thus understanding the circulation at the landing site is vital. Perseverance landed at longitude 77.45°E and latitude 18.44°N, close to the interior western rim of the ~45-km-wide Jezero crater, which itself sits on the interior northwest slopes of the ~1350-km-wide Isidis basin (Fig. 1, C and D). In situ wind data confirm atmospheric model predictions (*27*, *28*) that Jezero crater wind directions are driven primarily by regional (Isidis basin) and local (crater rim) slope flows, resulting in a reversal of wind direction twice per Mars day (sol). Daytime wind speeds vary hugely on subhourly time scales because of convective activity, but both hourly mean and maximum wind speeds are generally much stronger than those at night (Fig. 1A). Winds blow, on average, from the east-southeast from midmorning to sunset (Fig. 1B) and are more southerly earlier and more easterly later in the day. The pattern of daytime winds is very similar to that predicted by both atmospheric models that resolve the crater slopes and those that do not; see, e.g., figures 2 and 6 found in (*27*). This suggests that daytime winds are driven primarily by deep, strong, regional-scale Isidis basin upslope flows, with limited impact of the crater slope during the daytime period, with its thick planetary boundary layer (PBL) and thus with flows that are not confined close to the surface. However, closer inspection of the data during the midafternoon reveals a slight decrease in wind speed, which is also found in the crater-resolving simulations of (*27*, *28*). Movie S1 shows horizontal winds from a 1.4-km-resolution simulation using the Mars Weather Research and Forecasting (MarsWRF) mesoscale model (*29*) and suggests that the daytime regional flows are slightly deflected around the western crater rim and are partially blocked from entering Jezero—especially after 14:00—by opposing slope flows inside the crater on the southeast rim. Hence, although regional-scale slope flows appear to dominate during the daytime, local crater slopes likely explain the midafternoon wind speed dip seen in the data.

The global-scale Hadley circulation and large-scale planetary waves (e.g., thermal tides) must also certainly affect winds, but their influence is less obvious. Modeling (*27*, *28*) predicted that as Mars approached L_s = 90°, daytime winds would become more southerly than at the start of the mission (L_s ~ 5°). This is due to upwelling at low latitudes and downwelling at mid-latitudes around equinox, which produces a near-surface return flow from north to south at Jezero's location, whereas, at northern summer solstice, there is upwelling at northern mid-latitudes and downwelling at southern mid-latitudes, which produces a near-surface return flow from south to north. However, more work is needed to clearly identify such a shift in the observed wind directions up to sol 216 (L_s ~ 105°), in part because routine wind measurement did not begin until L_s ~ 20°. Similarly, the influence of thermal tides is difficult to disentangle from other factors but is expected to amplify during periods of high dust opacity, as observed by previous surface missions (*30*–*32*).

Although wind stress (hence the ability to transport sand or raise dust, if available) increases with atmospheric density, which is greater at night, the dominance of daytime wind speeds over those at night translates to estimated net sand transport toward 276°—i.e., from slightly south of east—over the first 216 sols of the mission; see Materials and Methods for a description of how wind stresses and sand fluxes are estimated from MEDA wind, pressure, and temperature data. This sand transport direction is consistent with orbital observations of active sand transport from roughly the east-southeast in and around Jezero crater (*27*, *28*) and with Perseverance observations of wind tails in Navcam and Mastcam-Z images (Fig. 2, A and B).

At night, winds since landing blow on average from the west-northwest, similar to the expected directions of nighttime downslope flows due to both the Isidis basin and Jezero crater slopes. While Isidis basin slope flows are predicted to increase in strength until sunrise, however, the observed wind minimum around 03:00 local true solar time (LTST) is only found in atmospheric models that resolve Jezero crater's rim (fig. S1) (*27*, *28*). As shown in Fig. 1 (E to G) and movie S1, in these models, the rim blocks the regional downslope flows, which are relatively shallow as a result of the thin PBL at night, but develops its own strong downslope winds; these flows extend to the rover's current location earlier in the night but then intensify and concentrate on the rim after ~01:30, causing wind speeds to decrease at the rover's location, consistent with observations. As Perseverance drives toward the crater rim, we expect nighttime wind

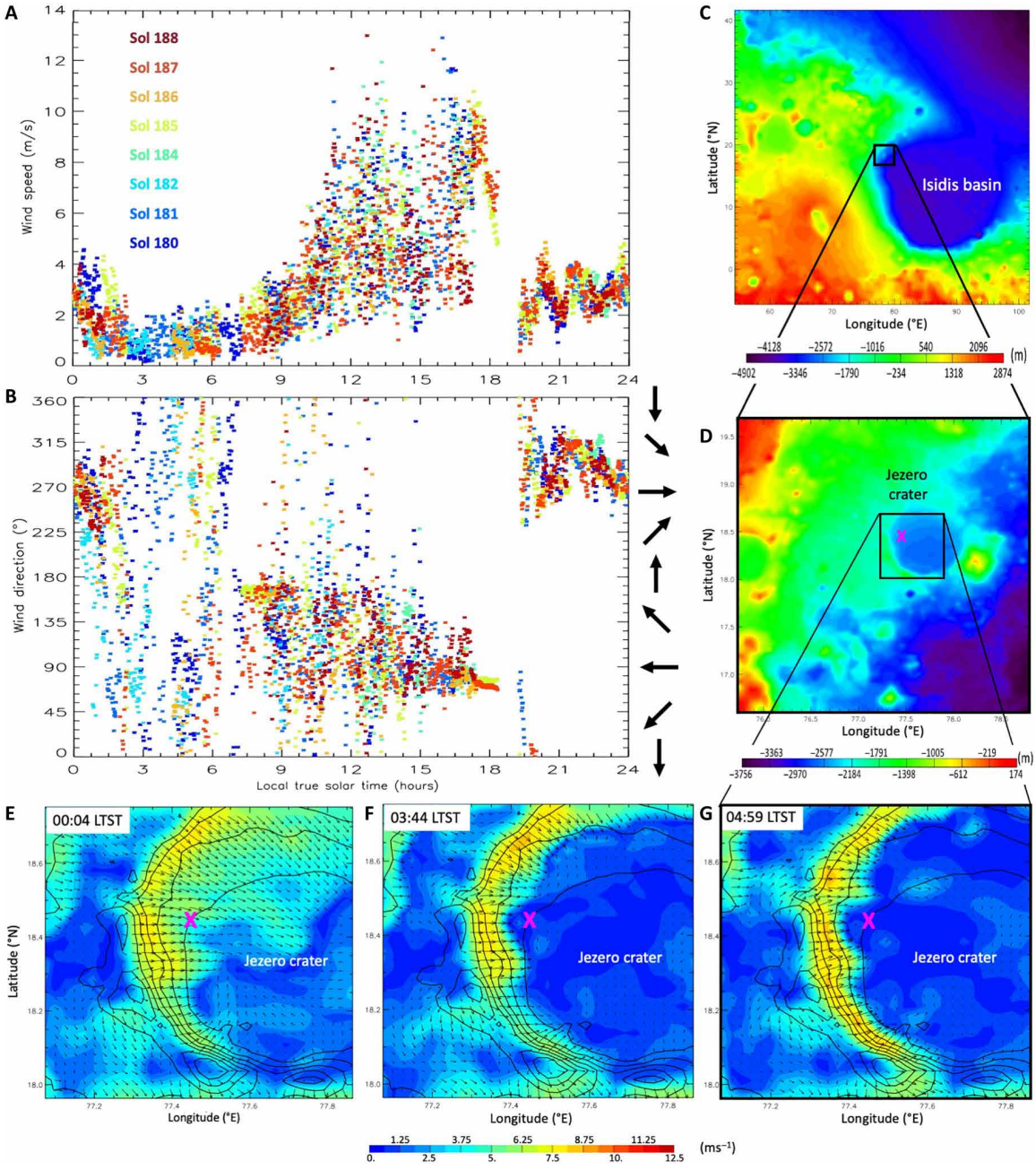

Fig. 1. Observed winds, regional and local topography, and modeled local slope control at night. Minute-averaged horizontal (**A**) wind speed and (**B**) direction the wind blows from at 1.45 m, observed by MEDA over 8 sols at $L_s \sim 90°$. (**C** and **D**) Location of landing site relative to Jezero crater and Isidis basin, showing (C) regional and (D) local scale topography. (**E** to **G**) Intensification and concentration of crater rim downslope flows from midnight to 5 a.m. local true solar time (LTST), shown as wind speed (shading) and vectors (arrows), simulated by the MarsWRF mesoscale model. Topography is shown as black contours, and the landing site is marked with a pink X.

speeds to increase substantially. This could potentially result in nighttime aeolian activity dominating, resulting in net sand transport from the west-northwest.

Fluting in ventifacts observed by Perseverance along its traverse (Fig. 2, C and D) already indicates dominant transport from the west-northwest (Fig. 2B), which is consistent with nighttime wind directions but inconsistent with wind speeds being much larger during the daytime at all locations and seasons observed to date. While it is possible that the circulation will differ in seasons we have yet to observe, the winds predicted by crater-resolving models appear to agree well with the seasons observed to date [e.g., fig. S1; (*27*, *28*)] and do not predict a seasonal shift in wind patterns (or net sand transport direction) large enough to explain the observed ventifact orientations (*27*, *28*). This suggests that the ventifacts formed either during anomalous weather conditions that modify the circulation pattern (a likely example would be regional or global dust storms, the impact of which on Jezero crater winds has not yet been explored in models) or during a past climate epoch. In the latter case, a strengthening of

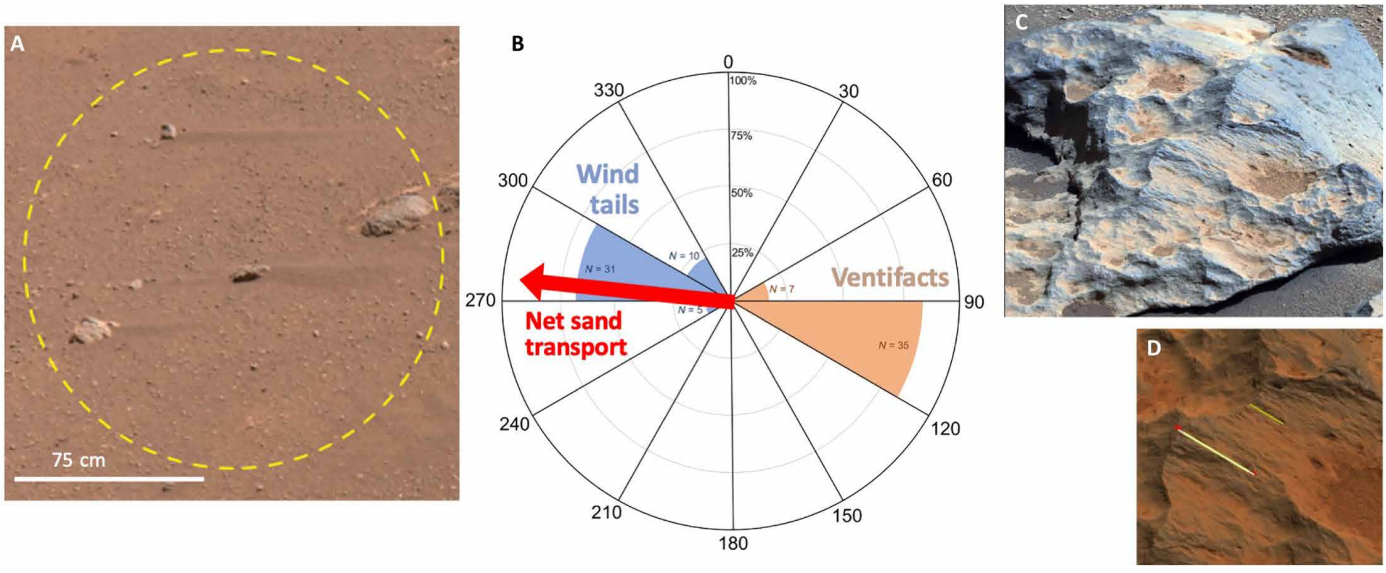

Fig. 2. Aeolian features and net sand transport direction over the first 216 sols. (**A**) "Wind tails" of sandy regolith extending from small rocks indicate wind-driven sand transport directions, as seen in this portion of a Navcam image taken on sol 32. (**B**) Rose diagram showing the orientation of wind tails (blue) and ventifacts (orange) observed along the rover traverse, as well as net sand transport estimated from MEDA winds and air densities (red arrow) over the first 216 sols. (**C**) A ventifact imaged by Mastcam-Z. (**D**) An example of azimuth measurements of flutes, from which the transport direction of abrading grains is inferred.

the northern winter Hadley circulation at higher obliquities, and of its associated north-to-south surface return flow, could potentially weaken daytime winds from roughly the southeast and enhance nighttime winds from roughly the northwest (perhaps enabling regional winds to penetrate into Jezero at night), shifting the dominant sand transport direction.

Rare "gust lifting" events are linked to the passage of convection cells

In Perseverance's first 216 sols, Navcam took 30 time-lapse movies and 49 surveys (five triplets of images taken in five directions clockwise around the rover, evenly spaced from north) designed to search for dust devils and dust lifting. Of these observations, three surveys show dust lifting by nonvortex wind gusts: on sols 117, 121, and 159 (L_s ~ 60°, 62°, and 79°) at 12:46, 11:56, and 15:32 LTST, respectively. These "gust lifting" events were likely present in both Gusev and Gale craters and imaged by Spirit and Curiosity cameras, respectively, but were not reported because of a lack of certainty over their origin. For example, in Gale crater, most candidates could also have been caused by a fading dust devil or by a dust devil partly hidden by topography. By contrast, the scale and context of the events seen in Jezero crater make it clear that they are driven by wind gusts and are not related to dust devils. Observations of the sol 117 gust lifting event, by far the largest of the three, are shown in Figs. 3 and 4 and in figs. S2 and S4. On the basis of the relationship of the dust clouds to surface features with known locations (Fig. 3A), the first, north-centered triplet of images (Fig. 3, B to D) shows dust being lifted, in a line running approximately north to south, over about half a minute. Regions of active dust lifting cannot be clearly differentiated from those with dust blowing over them, but we estimate a lifting area of at least 4 km^2. The fifth image triplet, 5 min later and centered just north of west, shows a dust cloud moving away over the delta to the northwest of the rover (fig. S2C). This is consistent with dust raised in the first image (Fig. 3B) being blown toward the west-northwest by the observed wind direction at this time (from the east-southeast, as shown in Fig. 4A).

Data from MEDA's RDS photodiodes (Fig. 4F) provide a more complete picture of dust activity during this event. The vertical field of view (FOV) of the RDS lateral sensors is ~20° to 30° above the horizontal, with azimuthal pointing as shown in Fig. 3E; hence, their signals can be interpreted as follows: Dust is raised and forms low dust clouds, producing the small lat6 and larger lat7 initial peaks; as lifting ceases, the dust is blown away at low altitudes to the west-northwest, moving sideways out of the lat6 FOV and below the lat7 FOV; and as the dust cloud reaches the delta front, it rises and moves fully into the lat7 FOV and then moves below it again as it continues to travel away from the rover, producing the large, long, and smooth second lat7 peak. Peaks in the roughly south-pointing lat2 and upward-pointing top7 sensors, coinciding with the first image triplet, seem unlikely to have been produced by the dust imaged in Fig. 3 (B to D) but could be due to dust raised by a previous gust front, passing close by the rover to the south/southwest. The lat4 signal coincides with diffuse dust activity to the east in the second image triplet (fig. S2B).

It is difficult to determine exact dust lifting locations or cloud heights from the images, but if we assume that dust in Fig. 3B was lifted no closer to the rover than point 5 on Fig. 3A and interpret the later increase in the RDS lat7 signal (Fig. 4F), ~2.25 min after the first image, as resulting from the dust cloud lifting up over the 65-m-high delta ~1.3 km away to the west-northwest, we obtain a speed of 9.6 m s^{-1}. This is larger than the average observed near-surface wind speed at the rover over this period, which is ~7 m s^{-1} over the entire hour shown in Fig. 4B or ~6 m s^{-1} over the second half of it. However, the dust cloud must have achieved a height of at least 65 m to pass over the delta, and wind speeds are expected to increase with height at this time of sol; for example, MarsWRF modeling indicates that they are typically ~50% stronger at 100 m than at 1.5 m (fig. S3). Therefore, the estimated speed at which the

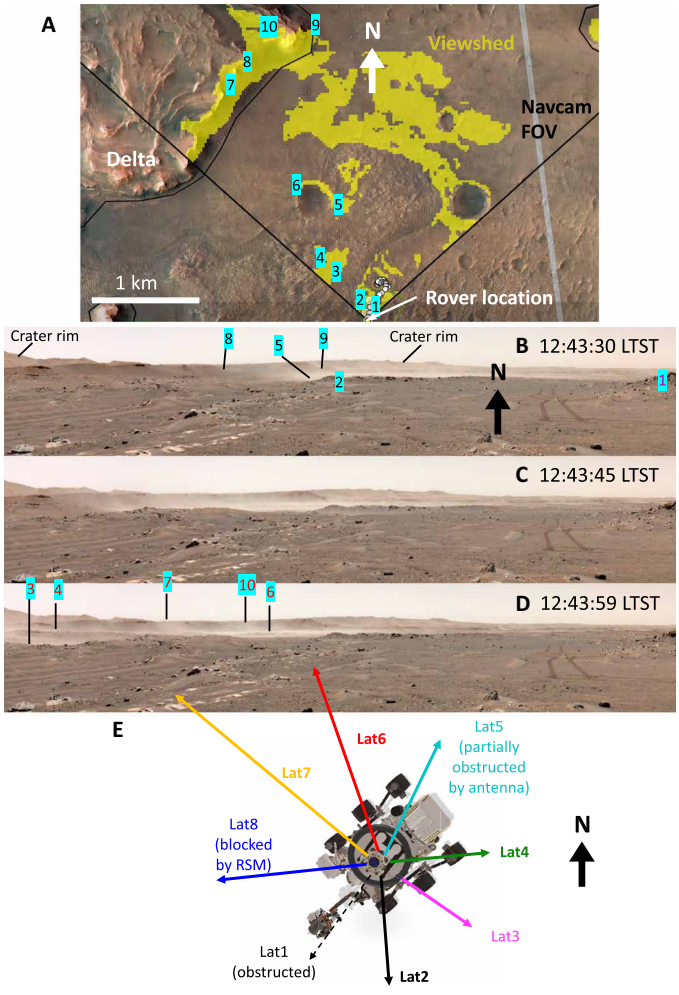

Fig. 3. The sol 117 gust lifting event in imaging. (**A**) Features used to track the path of dust lifting/transport; yellow shading shows the "viewshed" (the surface that is line-of-sight visible) from the rover's position. (**B** to **D**) The first, north-centered triplet of Navcam images, spaced ~14 s apart. Note that the right side of each image has been trimmed. (**E**) Azimuthal pointing of MEDA's RDS photodiodes on this sol.

cloud has traveled is consistent with the observed near-surface wind speeds at the rover.

All imaged gust lifting events to date occurred during the period of strong convective activity from ~10:30 to 16:00 LTST, which manifests as large temporal variability in wind speed (Figs. 1A, 4B, and 5A), temperature (Fig. 4, C and E), and other meteorological time series. On sol 117, this included a sequence of 24 SuperCam microphone recordings (fig. S4). The microphone signal is sensitive to the product of wind speed and its standard deviation (SD) (*33*), and two recordings made during the largest peaks in the MEDA wind data were strongly saturated (Fig. 4B and fig. S4), corroborating them as particularly intense and variable winds. The time scale of the variations (shown for winds in Fig. 5A) is consistent with the walls of convection cells passing overhead ~4 to 7 times per hour (periods of 8.6 to 15 min), advected by the large-scale daytime upslope winds. Similar activity was previously reported for the InSight landing site in Elysium Planitia (*34*, *35*), albeit with fewer peaks per hour (periods of 25 to 33 min), and has long been predicted for Mars by analogy with observations of meteorological time series in Earth's deserts (*36*) and in large eddy simulations (LES) of the daytime convective Martian atmosphere (*29*, *37*, *38*). These cells consist of strong, warm updrafts concentrated in narrow cell walls and weaker, cooler downdrafts in cell centers, with surface winds blowing toward the walls to conserve mass. As convection cells are advected over the region, the background and cellular near-surface winds have the same direction behind the leading cell wall and combine constructively to produce peak wind speeds there.

This can also be seen in the wind field of the MarsWRF mesoscale simulation, as shown in Fig. 5B and movie S1. While that simulation is marginal in terms of resolution for the scale of these cells (which have widths of ~6 to 7 km), the structure and sizing of the cells by this time of sol are confirmed by results from a 10-m-resolution MarsWRF LES run with imposed background winds based on the mesoscale model output, as shown in fig. S5. On the basis of the observed time scales of variations and the mean wind speeds over the same periods (Fig. 5A), typical cell widths in the direction of motion are estimated to be ~2.8 to 5 km. This is lower than the ~6- to 7-km cell widths found in the mesoscale and LES atmospheric simulations (Fig. 5B, fig. S5, and movie S1). Furthermore, PBL depth is expected to scale with cell width (*39*)—and does so very closely in the mesoscale and LES models—so this could be interpreted as suggesting that lower PBL depths are present in Jezero crater than are predicted. However, it should be noted that there are multiple scales of convection cells and structures in the convective boundary layer, and while the PBL depth will scale with the largest of them, the mixture may result in multiple or fragmented gust fronts (as shown in, e.g., the middle row of fig. S5).

As would be expected if they follow passage of a cell wall, the peaks in wind speed occur 1 to 2 min after a warming in surface temperature (Fig. 4E) and air temperature (Fig. 4C). The second large wind peak, 2 min before the first Navcam image, also coincides with a shallow, long-duration pressure drop (Fig. 4D). While cell walls are associated with updrafts, hence pressure drops might be expected to precede peak surface winds, the pressure signal is vertically integrated (i.e., depends on the cell's vertical tilt) and may not coincide with other surface signals (fig. S4) (*40*). We therefore hypothesize that gust lifting events are triggered by strong winds aligned in gust fronts behind the leading wall of strong convection cells, with these fronts (on average) perpendicular to the background wind direction. This hypothesis is consistent with the pattern of dust lifting and transport observed on sol 117 (Fig. 3). Over the period shown in Fig. 4, the mean wind direction was toward the west-northwest at a mean speed of ~7 m/s, while the dust lifting was consistent with strong winds along a gust front oriented roughly perpendicular to this wind direction.

Output from the high-resolution MarsWRF LES is used to calculate dust lifting for a threshold wind stress of 0.008 Pa and shows similar gust lifting events occurring along gust fronts (Fig. 5C and fig. S4). This threshold value corresponds to instantaneous wind speeds of between ~7 and 12 m s^{-1} at 1.5-m height in the LES, at the time of day shown in Fig. 5C. This is substantially lower than the peak wind speeds measured by MEDA, but peak wind speeds in the LES are generally lower than observed, very rarely exceeding 12 m s^{-1} (although a peak of 22 m s^{-1} is produced at the peak of the gust lifting event). Thus, the threshold of 0.008 Pa was chosen to reproduce roughly the observed balance in occurrence between dust lifting by vortex winds and dust lifting by wind gusts associated with fronts, with more than 25 large dust devils but only one large gust lifting

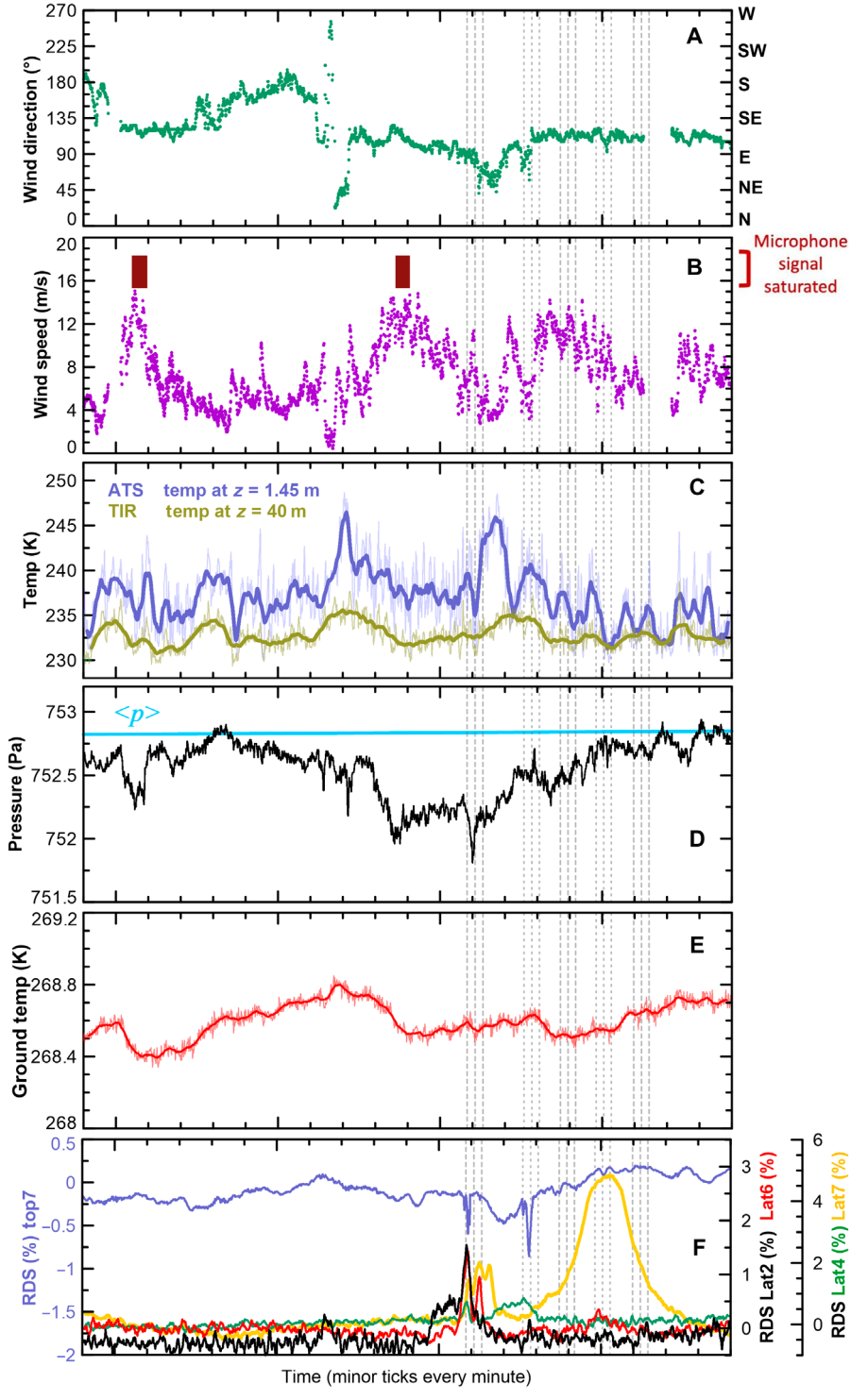

Fig. 4. The sol 117 gust lifting event in meteorological time series. (**A** to **E**) Time series of meteorological data over 20 min surrounding the sol 117 Navcam survey, with the timing of the five image triplets shown by vertical dotted lines. (A) MEDA direction that wind blows from. (B) MEDA wind speeds (purple) and periods with saturated SuperCam microphone signals (red boxes). (C) MEDA 1-Hz (thin lines) and 15-s running-average smoothed (thick lines) air temperature at 1.45 m (blue) and ~40 m (chartreuse). (D) MEDA surface pressure (black line) and an indication of the longer-term trend in pressure over the surrounding period (cyan). (E) As in (C) but showing MEDA surface temperature. (**F**) Percentage change in SW radiation measured by MEDA's RDS top7 (blue), lat2 (black), lat4 (green), lat6 (red), and lat7 (yellow) photodiodes.

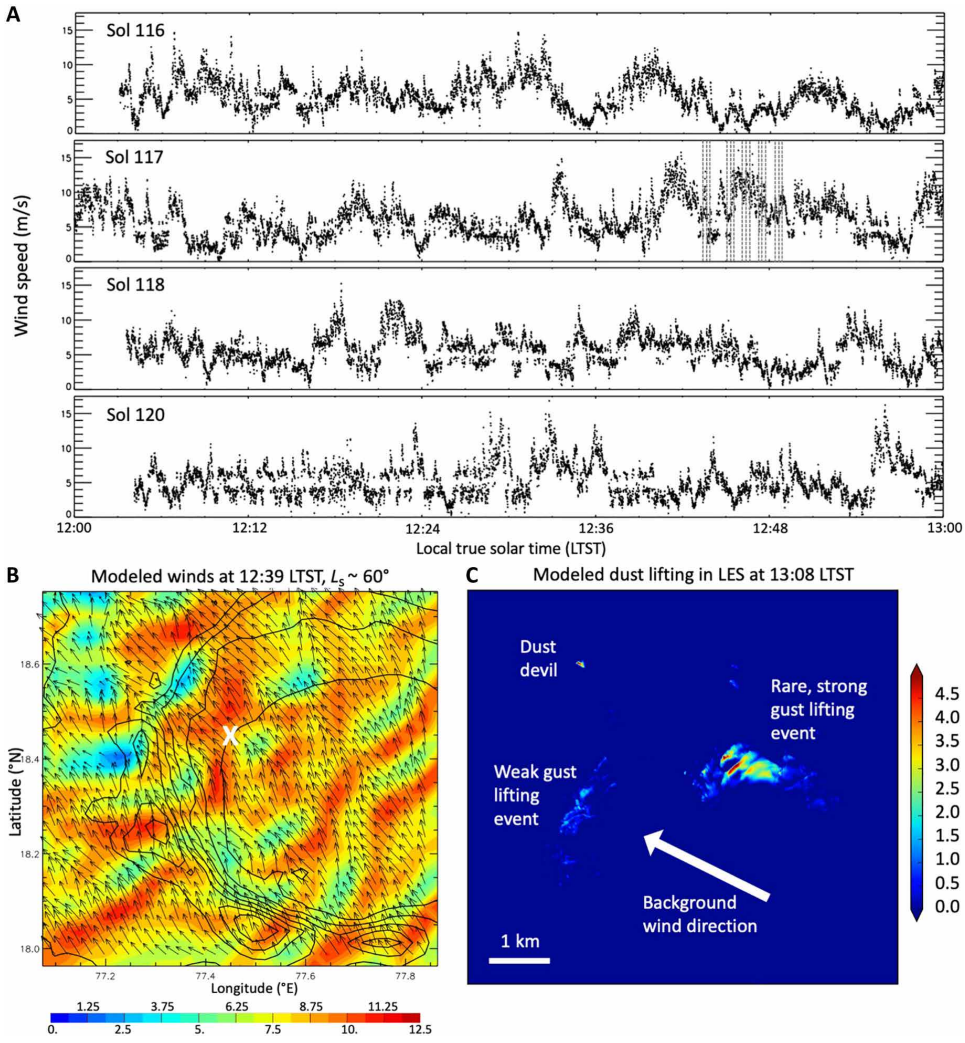

Fig. 5. Daytime winds and simulated gust lifting in Jezero crater around sol 117. (**A**) MEDA 12:00 to 13:00 instantaneous 2-Hz wind speeds for sols 116 to 118 and 120. (**B**) As in Fig. 1 (E to G) but now showing daytime convection cells being advected over Jezero crater at 12:39 LTST at L_s ~ 60°. (**C**) Snapshot of lifted dust flux (in arbitrary units) at 13:08 LTST in a MarsWRF LES of Jezero crater.

event in this sol over the entire 10-km^2 LES domain. The large range in wind speeds corresponding to this threshold value is because wind stress is given by atmospheric density × u_*^2, where u_* is the drag velocity, and the relationship between u_* and wind speed at a given height depends on the atmospheric stability and hence the vertical wind profile. This highlights the importance of considering the most physical quantity—i.e., wind stress—rather than wind speed when discussing threshold conditions, if possible. To date, however, direct measurements of u_* have never been made on Mars, and only one attempt has been made to measure u_* indirectly (*41*), making wind stress estimates and comparisons far more difficult.

We speculate that a gust front responsible for the second large wind gust shown in Fig. 4B intensified shortly after it passed the rover, exceeding the threshold wind and producing the observed dust lifting event. These results suggest that gust lifting in Jezero crater is produced by gust fronts with wind speeds exceeding a threshold value that is greater than ~15 m s^{-1} by some unknown amount. We comment on the significance of this value, and other estimations of threshold limits, in Discussion below. Recent modeling of turbulent dust lifting in terrestrial deserts involves the use of LES to parameterize dust injection schemes in global and mesoscale models, and these LES—with dust lifting by wind stress enabled at turbulent scales—produce very similar results to those produced here for Mars (*42*, *43*). This demonstrates the many analogies between dust lifting processes on Earth and Mars that may be explored by comparing field data and LES modeling from both planets.

Daytime convective vortices and dust devils are common in Jezero crater

While dust lifting by wind gusts appears relatively rare inside Jezero crater, dust lifting by convective vortices is very common, with dust devils appearing in 30% of movies and surveys designed to look for them, as well as frequently appearing in other images (fig. S6). Figure 6 shows a swarm of dust devils dancing across the crater floor in a Navcam movie, with intriguing dynamics as the two largest ones move toward and pass each other before fading. Convective vortices and thus dust devils typically form at the corners and edges of convection cells, where strong, warm updrafts exist. These areas

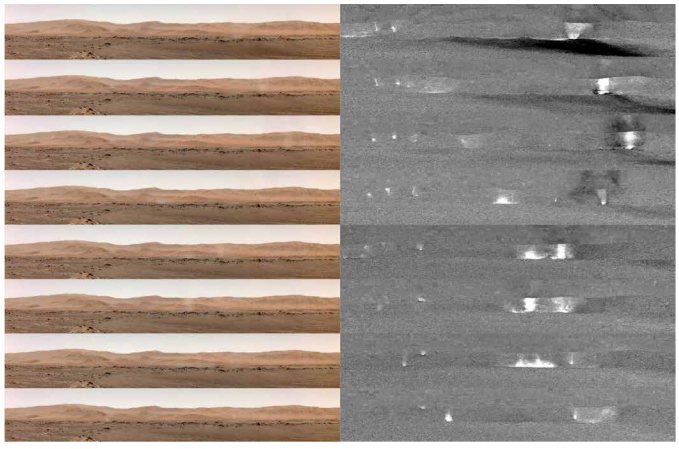

Fig. 6. Dancing dust devils on sol 148. (**Left**) Portion of Navcam dust devil movie (see movie S2) zooming in on vortices in the scene with images every ~28 s (every other frame) from 12:10:42 to 12:14:01 LTST. (**Right**) Difference between each image and the average enhancing changes in the scene, which include dust devils, their shadows, and surface dust changes.

of convection cells are thus associated with the strongest upwelling and the strongest horizontal gradients of temperature. The latter leads to baroclinic generation of horizontal vorticity, with some of these horizontal vortex tubes becoming buckled into the vertical (*44*). This is driven by rising air in the updrafts and general turbulent motions, both of which may be especially strong at vertices where cells intersect. Unlike Earth, on Mars, the production of vorticity is primarily driven by horizontal buoyancy variations rather than wind shear (*45*). The now-vertical vortices can then intensify by direct heating at the base or via merger with other vortices. As the pressure drop deepens, a spiral inflow of warm air strengthens single-celled vortices; a vortex may then further intensify to become two-celled, with an even deeper pressure drop surrounding a narrow downdraft at its inner, calm core (*46*).

The signature of all passing convective vortices is highly distinctive in MEDA wind and pressure data and is also distinguished in many events in temperature and longwave flux. Furthermore, MEDA's RDS photodiodes allow us to identify those vortices with significant dust content. Figure 7 shows the signature of a warm, dusty convective vortex passing the rover on sol 166. The large, short-duration pressure drop (Fig. 7A) and temperature changes (Fig. 7, B and C), closely spaced double peak in wind speed (Fig. 7D), rapid change in wind direction (Fig. 7E), and increase in downward longwave radiation (Fig. 7F) indicate a small, single-celled, but intense vortex (estimated to be ~20 to 30 m in diameter based on ambient wind speed) passing directly overhead. Furthermore, the decrease in downward (Fig. 7G) and reflected (Fig. 7H) shortwave radiation as the vortex blocks sunlight indicates that this vortex contains significant dust, while the order of the RDS lat2 (Fig. 7I) and lat4 (Fig. 7J) response is consistent with scattered light from a dusty vortex advected over the rover in ambient winds from the southeast or east-southeast, as shown by the cartoon in (Fig. 7K). Figure S7 shows the signature of a much larger (~600 m in diameter) vortex passing over the rover in sol 184, which includes a double pressure drop but is less dusty.

Analysis of MEDA pressure time series from the first 216 sols was performed using sliding windows of continuous pressure data over a given period. We detrended data from linear variations by fitting the first and last 15% of the data, as in (*47*). Pressure drops in the center of the period above a threshold (here 0.5 Pa) were identified and fit with a Gaussian, giving a quantitative description of the intensity and duration of the events. We used six different time windows from 60 to 900 s and looked at plots of all individual events to ensure that we did not miss vortices and did not add erroneous detections or incorrect durations. Correcting for gaps in coverage, results show more than four daytime vortex pressure drops exceeding 0.5 Pa detected on average per sol, with more than 1.15 vortices per hour detected on average at the peak time of day, 12:00 to 13:00 LTST (Fig. 8A). About 25% of vortices detected in this way also produced a decrease in the RDS top7 signal of >0.5%, indicating sufficient dust content to significantly block incoming sunlight (Fig. 8B). Note that this includes some dust devils passing on the opposite side of the rover to the sun, which are close and/or large enough to block significant scattered sunlight. However, some dust devils detected by MEDA's pressure sensor (PS) will have passed on that side of the rover at a large-enough distance to not block either the direct or scattered sunlight received by the sensor's wide FOV. Hence, 25% is a lower bound on the percentage of dusty vortices. This is similar to the percentage of dusty vortices found in a study covering only the first 89 sols of the mission (*48*). A full geometrical analysis involving all top and lateral sensors is needed to determine the true value, which will be between 25 and 50%. However, even 25% would make Jezero's vortices far dustier than observed by other missions, as described in the section comparing landing sites below.

What controls vortex dust lifting on Mars?

The large number of dusty vortices, combined with Perseverance's sensors, provides a valuable opportunity to study the cause of dust lifting by vortices on Mars.

Correlations between vortex characteristics and dust content

Dustier vortices typically have larger pressure drops [Fig. 8C; also compare Fig. 8 (A and B)] and maximum wind speeds (Fig. 8C), which are expected to be correlated [e.g., (*49*, *50*)]. This is consistent with stronger tangential winds—perhaps combined with a pressure drop suction effect—producing greater dust lifting. Exceptions, such as the two intense vortices on sol 188 (Fig. 8C), may have passed on the side of the rover opposite the sun and thus may only appear to be less dusty. However, there is little correlation between the approximate vortex diameter (inferred by multiplying the mean wind speed by the pressure drop duration; see example in fig. S7) and the pressure drop or dust content of the vortex (Fig. 8D). While the dustiest vortex observed to date (on sol 213) had an inferred diameter of nearly 300 m, the second dustiest (on sol 57) was less than 30 m across. In summary, the vortices lifting the most dust are often intense in terms of winds and pressure drops (for example, all dust devils causing more than a 15% drop in the RDS top7 signal have a $\Delta p > 2.5$ Pa and/or a wind speed of >18 m s^{-1}) but are not necessarily large in diameter.

Conditions required for local dust lifting by vortices

Local dust lifting was detected in association with vortex passage on four occasions over the first 216 sols, providing direct information on the threshold conditions needed to raise dust. On sols 57, 82, 166, and 211, MEDA's TIRS and RDS measured a sudden, significant, and persistent change in the ratio of the reflected and downward SW radiation immediately following passage of a vortex, indicating a change in surface albedo (Fig. 7L). Such a change can only be due to the removal of dust from the surface inside the TIRS

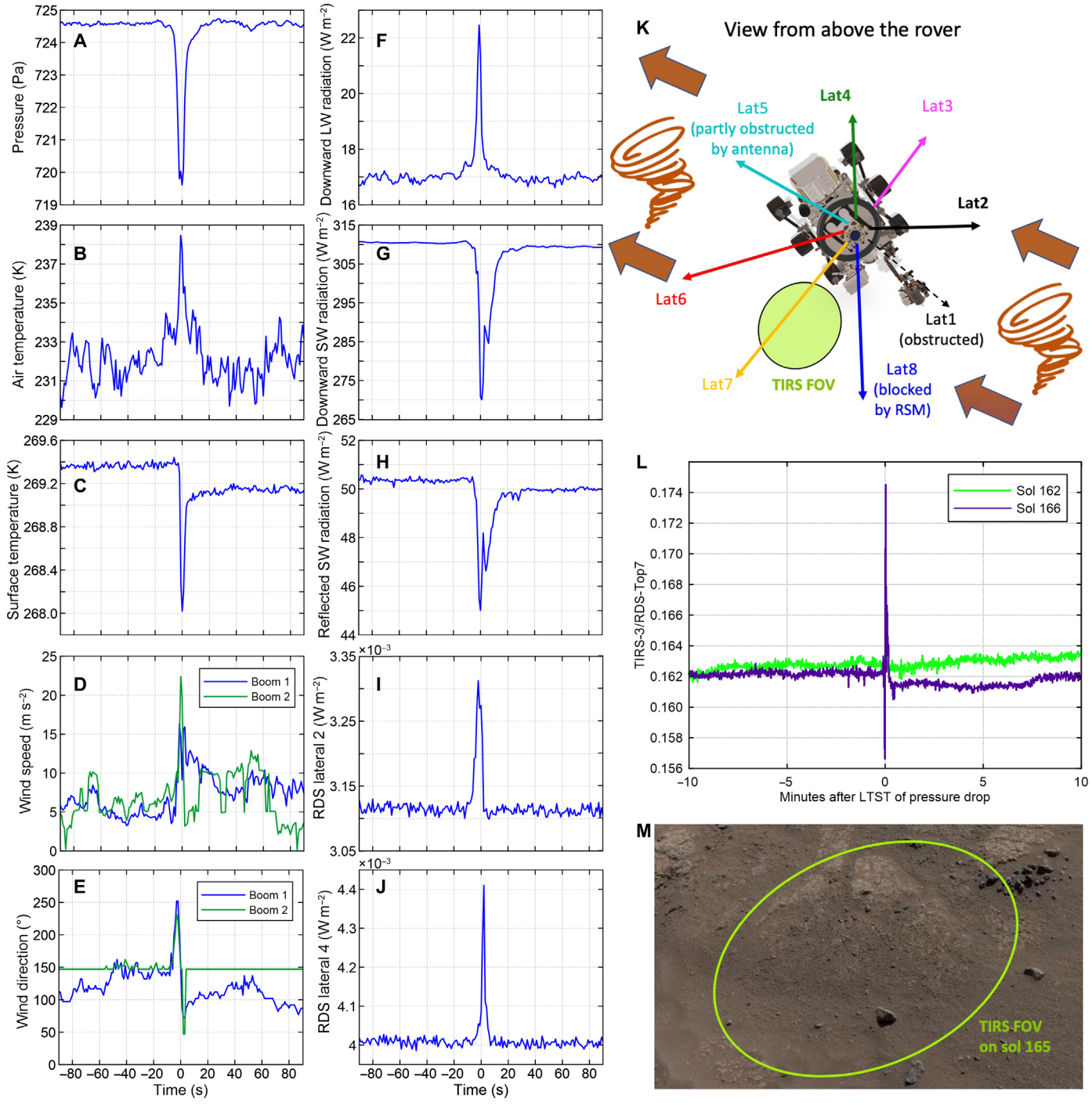

Fig. 7. The sol 166 vortex passage and dust lifting event. (**A** to **J**) MEDA data showing the signature of a warm, single-celled, dusty convective vortex passing over the rover (see text). (**K**) Cartoon of inferred dust devil path. (**L**) Sudden, persistent change in surface reflectance following vortex passage indicates dust lifting within the TIRS FOV (see text). (**M**) Navcam image of the TIRS FOV on sol 165 at the same location as during the vortex passage.

FOV (Fig. 7M). As shown by the purple bubbles in Fig. 8C, we find no local dust lifting by vortices for tangential wind speeds below 15 m s^{-1} (sol 57) or for central pressure drops below 2.6 Pa (sol 211). This minimum wind speed for dust lifting is comparable to that measured regularly in association with passing convection cells (e.g., Fig. 5A), yet such wind speeds alone have not been observed to raise dust locally, suggesting that the vortical nature of the encounter—such as the pressure drop effect—may be important. We explore the significance of these results for understanding dust lifting thresholds in Discussion below. Many vortices with much larger winds and/or pressure drops do not appear to raise dust locally, although, again, observational effects may have an impact. For example, the very

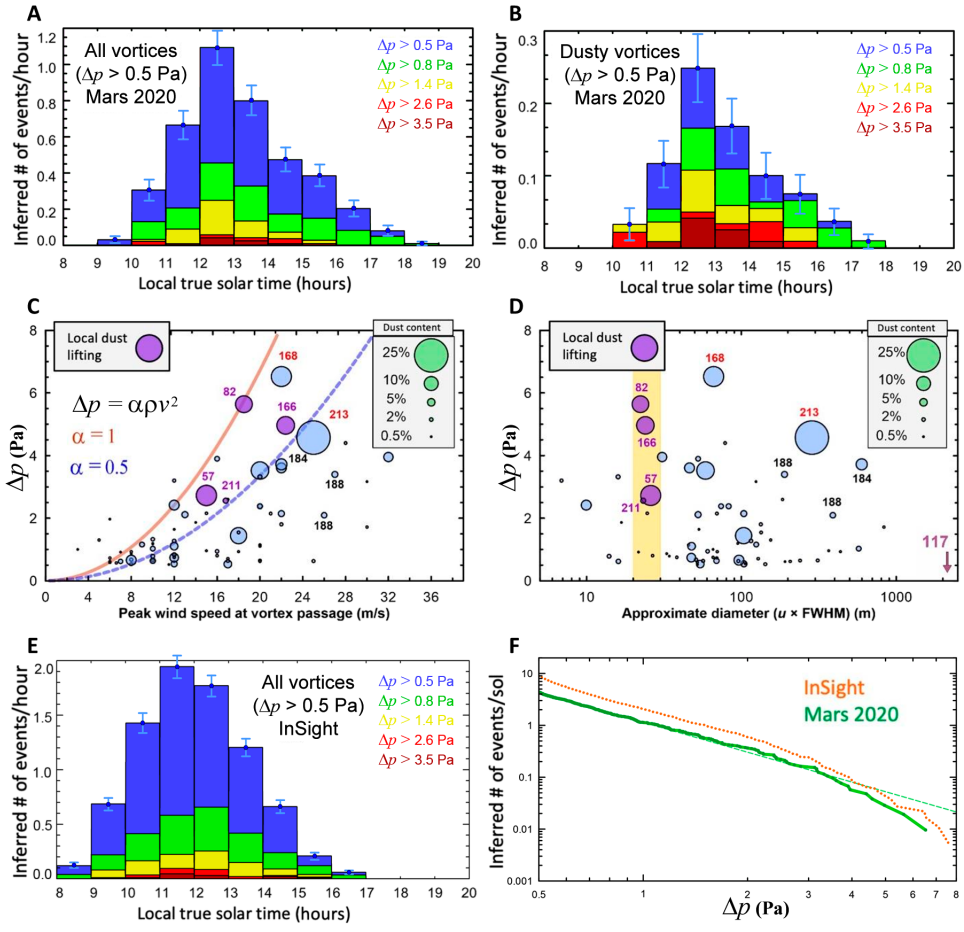

Fig. 8. Vortex and dust devil statistics in Jezero crater and comparison with same season at InSight. (**A**) Number and size distribution of vortex pressure drops of >0.5 Pa as a function of LTST, detected by Perseverance for L_s ~ 13° to 105°, corrected for gaps in data. Also shown are error bars based on a Monte Carlo analysis. (**B**) As in (A) but for dusty vortices, defined as a decrease of >0.5% in the RDS top7 signal. (**C**) Scatterplot showing peak wind speed versus largest pressure drop for all vortex events, with bubble size indicating dust content as percentage of decrease in RDS top7. Curved lines show the relationship between the maximum wind and the central pressure drop in a vortex assuming cyclostrophic balance (see text). Purple bubbles indicate the four events with local dust lifting detected (see text). (**D**) As in (C) but replacing the maximum wind speed with an approximate vortex diameter inferred from ambient wind speed and encounter duration. The spatial scale of the sol 117 gust lifting event is shown for comparison. (**E**) As in (A) but for same seasonal period at InSight. (**F**) Intensity distribution of pressure drops per sol detected by InSight and Perseverance, corrected for gaps in data.

dusty and intense sol 168 vortex occurred as the rover was moving, thus preventing the observation of any albedo change, while the dusty, intense sol 213 vortex occurred when a light-colored rock filled the TIRS FOV.

Comparison with other landing sites

Independent vortex and dust devil detections are available for this seasonal period at only two other places on Mars: Gale crater at ~4.5°S, location of the Curiosity rover, and Elysium Planitia at ~4.5°N, location of the InSight lander. Crucially, to enable a like-with-like comparison with Perseverance results, we consider only results obtained by applying an identical technique to that described above, with the same threshold pressure drop and examining a range of time windows, to data from both additional sites. For Curiosity, the peak number of vortex pressure drops of >0.5 Pa detected from early local spring through early local summer (L_s ~ 193° to 285° for this southern hemisphere site) never exceeds 0.6 per hour in the first three Mars years, while the number of vortices identified as being dusty [based on a decrease in solar radiation received by the rover's ultraviolet (UV) sensors] never exceeds 4% (*51*). This is consistent with the relatively low rate of dust devils imaged in Gale crater, although, after five Mars years on the surface, the number now exceeds several hundred. Much stronger dust devil activity was predicted in Jezero than in Gale crater in local summer by Newman *et al.* (*27*), based on the thermodynamical theory of Renno *et al.* (*49*), which was due mostly to the thinner PBL depth in Gale crater, although differences in sensible heat flux were also involved. Comparisons with these model predictions will be explored further in subsequent work.

By contrast, applying the same technique to the InSight pressure time series, we find that the number of vortex pressure drops of >0.5 Pa detected from L_s ~ 13° to 105° at the peak time of sol is nearly 2 per hour (Fig. 8E). If we compensate for the "advection effect" noted in (*34*, *52*)—i.e., that, given an identical rate of vortex production per unit area, stronger winds will advect more vortices over a stationary sensor in a set time—and correct for the mean daytime wind speed being roughly double at InSight in this season compared to Perseverance (~8 m s^{-1} versus ~4 m s^{-1}), then we find that nearly as many vortices are produced at InSight as in Jezero crater. The distribution of pressure drop durations also yields a similar

distribution of vortex diameters (background wind speed × event duration) at both sites (fig. S8), after we again account for the wind speed differences at the two sites. More importantly, the intensity of vortices at InSight and Perseverance is very similar, as shown by comparing the distribution of pressure drop magnitudes in Fig. 8 (A and E). Peak pressure drops of >8 Pa were observed during this period at InSight (*52*, *53*), compared to a peak of ~6.5 Pa at Perseverance (on sol 168), while peak wind speeds up to 31 m s^{-1} were observed at InSight in association with the convective vortices (*20*), similar to the peak wind speed (32 m s^{-1}) associated with vortices at Perseverance (Fig. 8C). At both sites, these vortices were inferred to cause surface changes seen in imaging, such as the motion of surface grains and appearance of nearby dust devil tracks at InSight (*19*, *20*) or the appearance of surface grains on the rover deck and motion of surface drill tailings at Perseverance (fig. S9).

However, despite these strong similarities in vortex number and characteristics between the two sites and contrary to the strong dust devil activity reported here by Perseverance, InSight has never imaged a dust devil in its more than 1.5 Mars years on the surface (as of early 2022), with cameras and solar array data showing that only 0.08 to 2% of vortices by area have significant optical contrasts with the background atmosphere (*35*). A possible explanation might involve greater surface dust abundance at Perseverance than at InSight. However, orbital and in situ data suggest that both InSight and Curiosity operate in regions of overall higher albedo and surface dust abundances than Perseverance (*54*–*56*). Furthermore, InSight has observed substantial net dust accumulation on its deck and solar panels since landing (*57*). This suggests that surface dust may be less abundant but more mobile—i.e., easier to raise—in Jezero crater, but a detailed hypothesis remains elusive.

Last, we note that the number of vortex pressure drops exceeding 0.5 Pa appears to peak earlier at InSight than at Perseverance, between 11 a.m. and noon versus noon and 1 p.m. [compare Fig. 8 (A and E)]. A similar behavior was noted in the thermodynamically based, prelanding predictions of dust devil activity of (*27*). By examining the contributions to dust devil activity, we find that this occurs because of a later peak in predicted values of sensible heat flux, which, in turn, results from a later peak in predicted wind speeds and hence drag velocity, u_*, at Perseverance than at InSight. This is consistent with the observed diurnal variation of wind speed at both sites, with InSight having strong winds from midmorning (*58*), whereas Perseverance wind speeds increase rather rapidly shortly before noon (Fig. 1A). However, this same wind speed variation will also affect vortex detection rates via the advection effect noted above, i.e., more vortices per hour will be advected past Perseverance from about noon onward compared to the mid- and late-morning. Hence, this may explain the earlier peak in detections at InSight. More investigation of all landed datasets is needed to untangle the different potential impacts of wind speed on vortex occurrence, including the possibility that winds above some threshold suppress the conversion of horizontal to vertical vorticity and thus decrease the number of vortices produced (*45*, *59*).

DISCUSSION

Dust devils and wind gusts could contribute equally to background dust lifting

An outstanding question for Mars is what maintains the background dust haze: dust devils or lifting by nonvortical wind stress. In total, we find that more than 30% of dust devil surveys or movies clearly contain dust devils, while a further 5% contain events whose origin is unclear. By comparison, only three gust lifting events were imaged by Navcam (found in <4% of surveys or movies) over the same period. However, the huge sol 117 gust lifting event may have raised dust over an area >4 km^2. By contrast, assuming a background wind of 4 m s^{-1} and lifetime of 6 min, the largest dust devil imaged (270 m in diameter) would have swept out an area $^1/_{10}$ as large. While the other two gust lifting events were far smaller and while larger dust devils were inferred from MEDA data (Fig. 8D), it is feasible that dust lifted by gust fronts might have equaled that lifted by vortices over this period, unless events such as that on sol 117 are exceedingly rare. More sols of data and more information on event size and duration—perhaps involving longer imaging sequences—are needed to assess whether dust devil or gust lifting dominates and to examine seasonal changes. This strongly motivates us to continue our search for both types of dust lifting events throughout the Mars 2020 mission.

Significance for understanding threshold conditions for dust lifting

A related outstanding question is what threshold conditions must be exceeded for sand motion or dust lifting to occur on Mars. We find that local dust lifting by vortices occurs only for tangential wind speeds above ~15 m s^{-1}, which was also the minimum wind speed reported in (*20*) at which surface darkening (inferred to be dust lifting by a passing vortex) was observed at InSight. However, the wind stress experienced by surface particles is the physically relevant threshold for dust lifting, and its value for a given wind speed at some height also depends on atmospheric stability (hence the vertical wind profile), surface roughness, and atmospheric density, all of which differ between Jezero crater and InSight's landing site. The ability to measure u_* and hence wind stress directly—via eddy correlation measurements enabled by high-frequency, high-precision three-dimensional (3D) wind sensors—would be a huge boon for future missions. Furthermore, it should be clear that winds of 15 m s^{-1} have been observed at some point by most surface missions to carry wind sensors (*19*, *20*, *60*–*62*) but have not been observed to raise dust outside of vortex encounters or to move sand. While Perseverance measured wind speeds of 15 m s^{-1} shortly before imaging huge gust lifting activity, no dust was raised locally. Combined with a lack of similar events either imaged or detected by MEDA RDS in most periods with similarly strong wind speeds, we assume that the gust front strengthened after passing over the rover; hence, the winds associated with dust lifting are unknown. Thus, a notional 15-m s^{-1} threshold appears limited to dust lifting by a vortex, in which case other factors are at work, including a "pressure drop" effect. Further analysis of vortex encounters and their associated wind speeds, pressure drops, and other characteristics will improve our statistics on the conditions needed for local dust lifting to occur. In addition, although these have been rare to date, we hope to experience a gust lifting event at the rover's exact location in the future, enabling us to measure wind conditions associated with local dust removal and thus provide important information on thresholds for nonvortex dust lifting.

Why is Jezero crater so active compared to most other landing sites?

Wind patterns in Jezero crater are generally consistent with prelanding predictions, with strong daytime winds largely controlled by convection

cells superimposed on regional, Isidis basin–scale slope winds, and weaker nighttime winds, suggesting blocking of regional winds by local crater slopes. However, the ability of gust fronts associated with convection cells to—albeit rarely—raise large amounts of dust was not identified prelanding and differs from observations at all prior landing sites. Furthermore, while substantial vortex activity was expected on the basis of thermodynamical arguments, the fraction of vortices that are dusty is far higher than at all previous sites for which the estimation of dusty versus dust-free vortices was possible (Spirit rover imaged a large number of dust devils but carried no pressure sensor). The contrast with InSight is particularly notable, as a site that has a roughly equivalent size, number, and intensity (in terms of winds and pressure drops) of vortices to Jezero, but has yet to definitively detect any dust devils. Identifying the cause of this difference will have major implications for understanding dust lifting across Mars. One remaining factor that may be responsible could be a difference in surface properties such as roughness, cohesion, and particle size distribution, including the aggregation of dust particles, all of which can affect the threshold for dust lifting. More detailed study of Jezero crater dust and of local surface conditions are needed to explore this further.

MATERIALS AND METHODS

MEDA overview

The MEDA sensor suite consists of a set of meteorological sensors that measure wind speed and direction, pressure, relative humidity, and atmospheric temperature at ~1.5 m above the surface and atmospheric temperature at 0.84 m above the surface. Furthermore, MEDA's RDS measures the direct and diffuse downward shortwave flux using 15 photodiodes, while MEDA's TIRS measures the reflected broadband shortwave flux; TIRS also measures the upward and downward broadband longwave flux, as well as measuring the upward and downward longwave flux in two narrower bands to give the infrared brightness temperature of the surface and of the atmosphere at ~40 m, respectively. Last, MEDA also includes the Skycam camera, which measures the column dust opacity twice per sol as well as taking images of clouds and dust. Skycam images are typically taken three (and up to seven) times per sol, while all other MEDA data are taken once or twice per second over about 13 hours in most sols. Complete details are provided in (*21*) and are summarized below for the sensors used in this work.

Air temperature from MEDA

The MEDA air temperature sensor (ATS) consists of three thermocouple sensors located at 1.45 m above the surface on the rover's remote sensing mast (RSM) and at 50°, 155°, and 290° around in azimuth with respect to the front of the rover, and two more thermocouple sensors located on either side of the rover front at 84 cm above the surface. At either height, the minimum of all or both sensors is typically used as the best estimate of the actual temperature at that height, which assumes that the rover's influence will generally warm the sensors above the temperature of the ambient air (*32*). However, more detailed analysis that combines ATS and wind sensor data is also possible, for example, to determine when a sensor is heated by air coming from the radioisotope thermoelectric generator (RTG). The ATS uses the same thermocouple wires as flown on the Phoenix lander, which were shown to have a temporal response of better than 0.8 s for all Mars conditions (*63*). The accuracy of the ATS is better than 0.9 K at the coldest temperatures expected and better than 0.65 K for temperatures above freezing (*21*).

Pressure from MEDA

The MEDA PS uses the same Vaisala Inc. Barocap® technology flown on the Mars Science Laboratory (MSL) Curiosity rover (*64*). Pressure moves the capacitor plates in a micromachined sensor head, changing its capacitance in a way that is only sensitive to pressure and temperature, which is also measured by Thermocap sensor heads. The PS consists of two pressure transducers (oscillators), P1 and P2, each with its own controlling electronics. Both P1 and P2 have two Thermocap sensor heads; P1 then has three Barocap® sensor heads, two with very good stability and resolution and the third with a very short warm-up time (under 2 s), while P2 has two of the latter type of Barocap® sensor heads. The primary science Barocap® is one of the high-stability sensors in P1 and has a resolution of better than 0.13 Pa, with a response time of better than 1 s.

Wind speed and direction from MEDA

The MEDA wind sensor (WS) is based on hot film anemometry and evolved from those flown as part of MSL's Rover Environmental Monitoring Station (REMS) and InSight's Temperature and Winds for InSight (TWINS) sensor suites. The WS consists of two short, horizontal booms mounted 120° of azimuth apart on the RSM at about 1.5 m above the surface. WS1 points at 6° clockwise with respect to directly out in front of the rover, with WS2 rotated 120° clockwise from this. Because of interference of flows as they pass around the RSM, each boom is unable to provide accurate measurements from certain directions, thus both are required to provide complete wind retrievals. Each WS boom carries six transducer boards, which are located around the boom. This improves redundancy in case of damage and also provides more nonhorizontal boards, which may be used to retrieve vertical winds. WS2 is also longer than on REMS to extend the sensing elements further from the rover's interference. Each WS board consists of four hot dice (in a two-by-two grid) and a cold (unheated) die. The latter measures the ambient temperature, while the hot dice are each maintained at a constant temperature difference to the ambient value, with the power needed to maintain this difference being measured. This is used to calculate the local gas thermal conductance at each hot die (*65*). When properly combined to cancel out radiation and other effects, these values provide the conductance in two orthogonal directions (longitudinal and transverse) for each board. These conductances from all six boards are then combined with wind tunnel calibration data to obtain the local wind speed and direction at each boom. The WS provides a resolution below 223 K of at least 0.5 m s^{-1} in speed in the 0- to 10-m s^{-1} range and of 1 m s^{-1} for wind speeds above 10 m s^{-1} up to 40 m s^{-1}; above 223 K, the resolution is better than 1.25 m s^{-1}. Wind data were taken at 2 Hz until sol 151, when the measurement frequency was reduced to 1 Hz, as for all other MEDA sensors.

For the results shown in this work, ambient wind speed and direction at any given moment is obtained by inferring which of the two WS booms was least affected by rover interference at that point. A boom selection algorithm is used, in which the wind data are taken from the boom that most closely points into the incoming wind. Spurious data are also identified by removing measurements following an increase in wind speed of more than 5 m s^{-1} compared to the immediately preceding measurement during a period of continuous measurement (i.e., within 1 s), with measurements used again after the

wind speed drops by more than 5 m s^{-1}. Note that this does not exclude sudden increases in wind speed related to vortices passing the rover, which display a very rapid but not instantaneous increase in wind speed. We estimate the uncertainties in wind speed and direction in the results shown here to be less than 1.5 m s^{-1} and 20°, respectively.

Radiative fluxes and surface and ~40-m air temperatures from MEDA

Located on the RSM at 1.5 m above the surface, TIRS is rotated 75° in the horizontal plane with respect to the rover's *z* axis. The FOV of the downward-looking channels covers an ellipse of about 3 m^2 in area (large enough for good signal-to-noise ratio but small enough to measure specific surface types in areas of variability) to the front side of the rover, which puts it ~3.75 m away from the RTG to mitigate thermal contamination (*66*). TIRS uses five Leibniz-IPHT TS-100 thermopiles, which were also used on MSL and on the Rosetta lander and which measure the radiative heat exchange between the observed targets and the transducer's sensing elements for temperatures from 138 to 313 K (*67*–*69*). The pointings, bandwidths, and performance of each sensor are given in table 10 found in (*21*). All have a FOV of ±20° and ±10° in the horizontal and vertical, respectively, and the upward/downward sensors are pointed at ±35°. Infrared (IR) band IR1 measures the broadband downward longwave from 6.5 to 30 μm, with an accuracy of ±1.2 to 6.9 W m^{-2} and a resolution of ±0.18 W m^{-2}. Band IR2 measures the air temperature at ~40 m (downward longwave from 14.5 to 15.5 μm), with an accuracy of ±2.83 K and a resolution of ±0.45 K. Band IR3 measures the broadband upward shortwave from 0.3 to 3 μm with an accuracy of ±3.7 to 9.6 W m^{-2} and a resolution of ±0.1 W m^{-2}. Band IR4 measures the broadband upward longwave from 6.5 to 30 μm with an accuracy of ±0.9 to 3.3 W m^{-2} and a resolution of ±0.13 W m^{-2}. Last, band IR5 measures the ground temperature (upward longwave from 8 to 14 μm) with an accuracy of ±0.75 K and a resolution of ±0.08 K.

The RDS–Discrete Photodetectors radiometer consists of two sets of eight photodiodes that measure sky brightness as a function of wavelength and azimuth (*70*). The first set (eight "top" channels) look directly upward and cover a range of UV, visible, and near-infrared wavelengths, which were chosen to study aerosol particle size, to discriminate dust from water ice, and to estimate ozone column abundance, as shown in table 22 found in (*21*). Most have a FOV of ±5° and cover a somewhat narrow wavelength band. The exception is the top7 sensor, which has a hemispheric (±90°) FOV and covers solar wavelengths from the UV to near-IR (190 to 1100 nm), making it sensitive to any changes in clouds or dust. The second set (eight lateral or "lat" channels) measure light at 750 ± 10 nm and point around the rover every 45° in azimuth, as shown in Figs. 3E and 7K as well as in table 23 found in (*21*), and at 20° above the horizontal (with the exception of lat8, which points at 35°), with a narrow FOV of ±5°. Note that the lat1 sensor is a calibration sensor and is permanently blocked by rover hardware. The accuracy of the RDS top7 channel is 5.6%, while the accuracy of each RDS lateral channel is 6.7%.

Extracting "albedo" from MEDA TIRS and RDS data

The ratio between the upwelling and downwelling solar radiation, measured by TIRS Band IR3 and by RDS top channel 7, respectively, is calculated as a proxy of the surface albedo. We note that the value might not reflect the actual surface albedo with high accuracy because further corrections based on the spectral responses of the sensors have not been performed at the time of writing. However, this ratio is adequate to detect rapid variations in surface reflectance due to changes in dust cover.

Navcam dust surveys and movies

Navcam dust devil surveys are imaging sequences designed to characterize the times and places of dust devil activity, as well as to gather information on their properties (such as size and advection speed) in some circumstances. While designed initially for dust devil monitoring, they have additionally captured several gust lifting events, as well as other aerosol phenomena (e.g., passing dust or water ice clouds).

Surveys comprise 15 images, taken in five sets of 3. Each triplet has a common aim with no RSM motion, and the images are used to filter for motion and determine the location and direction of any changing feature. The five different aims are offset by 72° (starting by pointing north and then rotating clockwise) to allow characterization of all visible landscape. The images are subframed and binned to keep the full 96° FOV of the camera (*23*) and preserve the horizon but avoid the area < 20 m from the rover and minimize downlink bandwidth.

Navcam dust devil "movies" are imaging sequences designed to characterize the motion and dust load of dust devils through repeat, time-lapse imaging of the same place. The movies discussed in this work are typically 5 to 7 min in duration and involve 21 frames. They also have 96° by 18° subframes.

Survey and movie processing involves the determination of a mean frame after some type of bright and dark exclusion for each pixel, with the method depending on the number of co-pointed frames. Each frame is then ratioed with the mean frame to observe motion. The sol 148 movie (Fig. 6) shows −6 to +6% brightness compared to the mean.

SuperCam microphone

The SuperCam microphone is located on the mast of the rover, close to the SuperCam laser head (*71*). Its main task is to listen to SuperCam laser-induced breakdown spectroscopy (LIBS) activities and use sound to help determine, for example, the hardness of rocks. It is also used to listen to other rover activities, such as the pump of the Mars Oxygen In-Situ Resource Utilization (ISRU) Experiment (MOXIE), and to helicopter flights. Furthermore, it is used for atmospheric science by providing high-frequency information on the turbulent atmosphere, including wind statistics and the potential detection of convective vortices and dust devils (*22*, *71*).

The microphone signal is sensitive to the product of wind speed and its SD and so will highlight/emphasize variable wind gusts. Figure S10 shows scatterplots of the root mean square of the SuperCam microphone signal in the 10- to 50-Hz bandwidth and the wind speed, wind SD, and product of the wind speed and SD (left to right). The wind speed data are from MEDA boom 1. The lower spread in the data for the product of wind speed and SD shows that both factors are important in producing signal power in the microphone data, as demonstrated in (*33*).

Net sand transport estimated from MEDA data

The direction of net sand transport shown by a red arrow in Fig. 2B is estimated using MEDA data up to sol 216 of the mission, covering L_s ~ 13° to 105°. We use MEDA winds at height z = 1.5 m above the surface to estimate the friction velocity, u_*, from the law of the wall for neutral conditions: $u(z) = u_* \ln(z/z_0)/k$, where Von Kármán's

constant $k = 0.4$. We initially assume a roughness height, $z_0 = 0.01$ m. We then assume that flux is proportional to $D \times u_*^2 (u_* - u_{*t})$, after (*72*), to calculate the sand transport direction for each valid MEDA measurement, where D is atmospheric density, given by $D = p/(R'T)$; p is pressure measured by MEDA; R' is the gas constant for Mars = 190 J kg^{-1} K^{-1}; and T is atmospheric temperature measured by MEDA at 1.45 m. To avoid reliance on a specific threshold for motion, we initially use a threshold friction velocity, $u_{*t} = 0$. We next sum the sand transport vectors over 1-hour bins and find the average in each 1-hour bin for every sol. We lastly combine these vectors, correcting for data gaps (i.e., missing 1-hour bins), to find the net sand transport direction over the complete period. A more sophisticated analysis in the future should use a full year's worth of data, correct for seasonal and time-of-sol biases in number of measurements, use a better estimation of roughness height in Jezero crater, calculate u_* by also considering the stability of the near-surface atmosphere at each time based on ATS measurements at multiple heights, and explore the impact on the net sand transport direction of assuming different threshold wind stresses, S_t, for motion, where $u_{*t} = \mathrm{sqrt}(S_t/D)$.

The MarsWRF multiscale model

The MarsWRF model (*27*, *29*, *73*–*75*) may be used to (i) simulate only the global circulation, (ii) simulate nested higher-resolution domains within a global context (acting as a two-way nested mesoscale model), or (iii) simulate microscale turbulent motions (in LES mode). The model includes the treatment of radiative transfer in the Martian atmosphere, including the effects of carbon dioxide gas and ices, aerosol dust, and water vapor and water ice (*76*, *77*). The model also includes fully interactive cycles of carbon dioxide, dust, and water; however, the simulations used here do not include the effects of water vapor or ice, and the time-evolving, 3D atmospheric dust distribution is prescribed using 3D evolving measurements of dust abundance retrieved from Mars Global Surveyor (MGS) Thermal Emission Spectrometer (TES) data, as described in (*27*). The model uses the Medium-Range Forecast (MRF) PBL scheme (*78*) to perform vertical mixing of heat and momentum, and a prognostic surface/subsurface scheme treats the surface-atmosphere exchange of momentum and heat and the diffusion of heat within a multilayer subsurface model (*29*). Surface property maps (albedo, thermal inertia, and surface roughness) are based on MGS datasets, as described in (*27*).

MarsWRF run in nested mesoscale mode for the Jezero crater region

In nested mesoscale mode, MarsWRF is run as a global model (domain 1) with four embedded "nests" (domains 2 to 5) centered on the Jezero crater region, each of which sits within its parent domain and covers a smaller area at three times the horizontal resolution; see figure 1 found in (*27*). The horizontal grid spacing in domain 1 is 2°, giving a horizontal grid spacing of ~1.4 km in domain 5 covering the region around Jezero crater. Figure 1 (C and D) here shows MarsWRF domains 2 and 5, respectively. Vertical grid A, as shown in table 4 found in (*74*), is used and consists of 43 layers from the surface to ~80 km, with greater vertical resolution in the lowest ~12 km of the atmosphere. The lowest three layers have their midpoint below 105 m and the lowest layer midpoint is at ~10 m above the surface. These nested simulations are run for 8 sols every 30° of L_s over a full Mars year, with the first sol of each simulation discarded as spin-up.

MarsWRF run in LES mode for Jezero crater conditions

In LES mode, MarsWRF is run at much higher spatial resolution, such that many small-scale eddies and their impact on circulation and transport are resolved (*29*, *40*). Thus, while the same radiative transfer and surface/subsurface schemes are used as in the nested mesoscale simulation, a PBL scheme is not needed. However, the LES does not resolve all motions down to the scales of dissipation (<<1 m), so a subgrid scale mixing parameterization is added, in which diffusivity and viscosity are based on the turbulent kinetic energy. The LES grid is treated as an idealized domain with doubly periodic boundary conditions. This can be thought of as creating an effectively infinite plane, although motions on scales larger than half the mesh extent are suppressed by the periodicity. The simulation for which results are shown here (Fig. 5C and fig. S5) uses a 10-m grid spacing over a region covering 10 km by 10 km and imposes constant values of topography, surface albedo, thermal emissivity, and subsurface thermal diffusivity across the entire domain, although these may be prescribed to vary based on observations. The simulation is located at the landing site coordinates and is initialized with background westerly winds, blowing to the east at a speed of 4 m s^{-1}, which persists as the averaged wind speed and direction over the entire simulation. Note that the orientation of the LES domain has no impact on the simulated dynamics; thus, to compare with observations, one can simply rotate the domain such that the imposed wind direction matches the average wind direction observed at that time of day (i.e., from roughly the west-northwest at night and from roughly the east-southeast during the day), as is done for Fig. 5C. The calculation of dust lifting in the LES is performed using the sand transport formula of (*72*), also described above, but with a threshold wind stress of 0.008 Pa, which is converted to a threshold friction velocity using the modeled atmospheric density.

Measuring orientations of surface aeolian features

Wind tails of sandy regolith extending from small rocks indicate wind-driven sand transport directions. Features such as these on flat ground away from large nearby obstacles (that could shield some wind azimuths) were measured during the first 200 sols of the mission to determine recent wind directions affecting loose surface materials. See data S4.

Flutes and other features of ventifacts typically occur on the upwind side of rocks, so that they slope upward downwind (*79*). Some rocks that stand well above the surrounding surface also show radiating patterns away from the upwind directions. See data S4.

Detecting vortex signatures in pressure data

Methodology

Vortex detections in pressure data vary hugely depending on both the minimum size of pressure drop chosen and the exact method used to detect this. It is therefore very important to use the same threshold and vortex detection method when comparing results at different locations, which is why we perform an analysis of the InSight pressure dataset despite this having already been investigated in previous work by other authors. Even if one surface mission carries a much more sensitive or higher-frequency pressure sensor than other missions, the threshold should be chosen such that events can be clearly differentiated from background pressure fluctuations in the least sensitive or lowest-frequency dataset. It is also very important to use a range of time windows to account for differences

in the duration of vortex detections at different locations and to catch all vortices (exceeding the threshold pressure drop) passing the rover regardless of the geometry of their passage. For example, two identical vortices passing with the same geometry will produce signals of very different durations if the background wind advecting them past the pressure sensor is very different.

We use here a detection algorithm modified from (*47*). The algorithm reads the data using a moving window of a fixed time duration and calculates a linear fit to the first and last 15% of the pressure signal disregarding the central 70% of the signal. The pressure signal, minus the linear fit, forms a detrended signal from the daily and seasonal variations of pressure. Whenever the central point of the detrended signal is at least −0.5 Pa (our detection threshold), we plot the pressure signal of the moving window and fit a Gaussian and a Lorenzian to the detrended signal to quantify the duration and intensity of the event. These fits do not need to be centered on the central point. The moving window advances by 1 s on each evaluation. Because the results depend on the time duration of the moving window, we perform several searches of the data with time windows of 60, 120, 180, 300, 600, and 900 s for Mars 2020. Each evaluation of the algorithm generates a catalog of events and a series of plots that are visually examined to remove spurious detections and select the time window that results in the best fit to each event. The basis of the catalog for Mars 2020 is the 300-s time window; other time windows provide only a small percentage of additional events or are used because they result in slightly better fits to events identified using the 300-s window. For InSight, which typically has larger wind speeds, the 120-s time window provides more detections, but time windows from 30 to 600 s are also examined. In both cases, errors in the properties of the vortices were estimated by comparing fits to individual events using different time windows. For intense events with pressure drops larger than 2.0 Pa, the magnitude of the pressure drop is precise to within 3%. The full width at half maximum of these intense events is precise to within 5% for events shorter than 20 s, but the error can grow to 20% for events that are weak, long, or noisy. For Mars 2020 data, the final consolidated results are used to generate plots of 15 min (or shorter if the event is close to the start or the end of an acquisition session) of all MEDA sensors. These are examined to quantify the properties of each event, such as the simultaneous detection of a change in airborne dust abundance, or fluctuations in wind speed and direction. Mars 2020 vortex detections are provided in data S1, with InSight results provided in data S2.

Choice of 0.5-Pa detection threshold

The detection threshold depends on the noise level of the detector and the amount of turbulence in the environment producing frequent pressure variations. For small-intensity pressure drops, their identification as vortices can be problematic. A 0.3-Pa detection threshold was used by Ellehoj *et al.* (*52*) for Phoenix data, while Spiga *et al.* (*34*) also used a threshold of 0.3 Pa for InSight data, although the first analysis by Banfield *et al.* (*58*) considered a more conservative threshold of 0.5 Pa. However, both InSight and Phoenix used sensors with lower error noise than those on Curiosity (REMS) or Mars 2020 (MEDA). A detection threshold of 0.5 Pa is typical in most analyses of REMS data (*17*, *47*, *51*, *75*). In particular, Kahanpää *et al.* (*17*) discuss the merits and difficulties of both thresholds for REMS data.

Our analysis of the pressure data leads us to conclude that the level of noise in the sensor and the typical variability at our location does not permit detection of all vortices with a threshold of 0.3 Pa. There are many of these low-intensity events and their analysis results in a similar daily distribution of activity, with an increased number of events that scales up to at least eight events detected per sol. While many are very clear, however, we believe that many more of these small events are hidden because of the combination of noise and environmental turbulence.

Errors in the statistics of the inferred number of vortices per hour in Fig. 8 can be estimated using a Monte Carlo analysis considering our inferred number of detections and sampling. We compare the number of detections with the number of hours observed at each of the 24 hours in a sol to compute an observed event rate. Then, we simulate how random events with a uniform distribution, and produced with the inferred event rate, would be detected in accumulated observations equal to the same number of hours. The statistics of over 500 simulations provides errors in event rate for all events with a pressure drop threshold of 0.5 Pa or larger, as shown by the error bars in Fig. 8. The Monte Carlo analysis indicates that these detection statistics are correct to within 5% of the detection rate at noon (1.13 ± 0.06 events per hour for $\Delta p > 0.5$ Pa) and increase smoothly to 35% or more in the early morning and late afternoon.

Detecting dust devil signatures in RDS data

Reductions in downward shortwave radiation measured by the full-sky FOV RDS top7 sensor are the best indicator of passage of a dust devil or dust cloud that blocks some sunlight from reaching the rover. The lateral sensors are also very useful for determining the location or path of a dust devil or cloud around the rover; however, their much narrower FOV makes these detections and their interpretation more complex and dependent on the rover–sun–dust devil/cloud geometry. While lateral sensor detections will be explored in future work, for this paper, we focus on detections by only the top7 sensor but acknowledge that some dust devils passing on the opposite side of the rover to the sun may have been missed, and thus, the fraction of vortices identified as containing significant dust may be underestimated.

Detections of drops in the RDS top7 sensor signal associated with simultaneous pressure drops were quantified by making linear fits to the RDS top7 sensor data over a 15-min window. These fits were used to detrend the linear variation in top7 values from varying illumination conditions as the position of the sun changed over the period. Errors in the quantification of the downward shortwave reduction depend on the characteristics of individual events and are around 0.2% for weak events and 1% for the strongest. Figure 8 and data S1 include only events with a top7 signal decrease of at least 0.5%.

We compared detections associated with pressure signatures, as described above and shown in data S1, and an independent analysis of the RDS top7 signals using a threshold of 0.4%, shown in data S3. The two datasets are largely consistent, despite the difference in threshold, with the RDS-only dataset showing additional events that may also be associated either with nonvortical dust clouds or with distant dust devils that are tall enough to affect top7 but too distant to have a strong signal in pressure data. Further analysis of these events, as well as all dust events detected in the lateral sensors only, will be presented in a future paper.

SUPPLEMENTARY MATERIALS

Supplementary material for this article is available at https://science.org/doi/10.1126/sciadv.abn3783

REFERENCES AND NOTES

1. S. Diniega, A. M. Bramson, B. Buratti, P. Buhler, D. M. Burr, M. Chojnacki, S. J. Conway, C. M. Dundas, C. J. Hansen, A. S. McEwen, M. G. A. Lapôtre, J. Levy, L. McKeown, S. Piqueux, G. Portyankina, C. Swann, T. N. Titus, J. M. Widmer, Modern Mars' geomorphological activity, driven by wind, frost, and gravity. *Geomorphology* **380**, 107627 (2021).
2. M. A. Szwast, M. I. Richardson, A. R. Vasavada, Surface dust redistribution on Mars as observed by the Mars Global Surveyor and Viking orbiters. *J. Geophys. Res.* **111**, E11008 (2006).
3. D. Viúdez-Moreiras, C. E. Newman, M. Torre, G. Martínez, S. Guzewich, M. Lemmon, J. Pla-García, M. D. Smith, A. M. Harri, M. Genzer, A. Vicente-Retortillo, A. Lepinette, J. A. Rodriguez-Manfredi, A. R. Vasavada, J. Gómez-Elvira, Effects of the MY34/2018 global dust storm as measured by MSL REMS in Gale crater. *J. Geophy. Res.* **124**, 1899–1912 (2019).
4. M. A. Kahre, J. R. Murphy, C. E. Newman, R. J. Wilson, B. A. Cantor, M. T. Lemmon, M. J. Wolff, The Mars dust cycle, in *The Atmosphere and Climate of Mars*, R. Haberle, R. T. Clancy, F. Forget, M. D. Smith, R. W. Zurek, Eds. (Cambridge Univ. Press, 2017), pp. 295–337.
5. R. Greeley, N. T. Bridges, R. O. Kuzmin, J. E. Laity, Terrestrial analogs to wind-related features at the Viking and Pathfinder landing sites on Mars. *J. Geophys. Res.* **107**, E1 (2002).
6. L. J. Martin, R. W. Zurek, An analysis of the history of dust activity on Mars. *J. Geophys. Res.* **98**, 3221–3246 (1993).
7. N. T. Bridges, F. Ayoub, J.-P. Avouac, S. Leprince, A. Lucas, S. Mattson, Earth-like sand fluxes on Mars. *Nature* **485**, 339–342 (2012).
8. M. M. Baker, M. G. A. Lapotre, M. E. Minitti, C. E. Newman, R. Sullivan, C. M. Weitz, D. M. Rubin, A. R. Vasavada, N. T. Bridges, K. W. Lewis, The Bagnold Dunes in southern summer: Active sediment transport on Mars observed by the Curiosity rover. *Geophys. Res. Lett.* **45**, 8853–8863 (2018).
9. R. Sullivan, J. F. Kok, Aeolian saltation on Mars at low wind speeds. *J. Geophys. Res.* **122**, 2111–2143 (2017).
10. C. Swann, D. J. Sherman, R. C. Ewing, Experimentally derived thresholds for windblown sand on Mars. *Geophys. Res. Lett.* **47**, e2019GL084484 (2020).
11. J. F. Kok, Difference in the wind speeds required for initiation versus continuation of sand transport on Mars: Implications for dunes and dust storms. *Phys. Rev. Lett.* **104**, 074502 (2010).
12. R. Sullivan, R. Arvidson, J. F. Bell III, R. Gellert, M. Golombek, R. Greeley, K. Herkenhoff, J. Johnson, S. Thompson, P. Whelley, J. Wray, Wind-driven particle mobility on Mars: Insights from Mars Exploration Rover observations at "El Dorado" and surroundings at Gusev Crater. *J. Geophys. Res.* **113**, E06S07 (2008).
13. G. Musiolik, M. Kruss, T. Demirci, B. Schrinski, J. Teiser, F. Daerden, M. D. Smith, L. Neary, G. Wurm, Saltation under Martian gravity and its influence on the global dust distribution. *Icarus* **306**, 25–31 (2018).
14. L. D. V. Neakrase, M. R. Balme, F. Esposito, T. Kelling, M. Klose, J. F. Kok, B. Marticorena, J. Merrison, M. Patel, G. Wurm, Particle lifting processes in dust devils. *Space Sci. Rev.* **203**, 347–376 (2016).
15. H. J. Moore, R. E. Hutton, G. D. Clow, C. R. Spitzer, "Physical properties of the surface materials at the Viking landing sites on Mars" (USGS Professional Paper 1389, 1987).
16. R. Greeley, D. A. Waller, N. A. Cabrol, G. A. Landis, M. T. Lemmon, L. D. V. Neakrase, M. Pendleton Hoffer, S. D. Thompson, P. L. Whelley, Gusev Crater, Mars: Observations of three dust devil seasons. *J. Geophys. Res.* **115**, E00F02 (2010).
17. H. Kahanpää, C. Newman, J. Moores, M. P. Zorzano, J. Martín-Torres, S. Navarro, A. Lepinette, B. Cantor, M. T. Lemmon, P. Valentín-Serrano, A. Ullán, W. Schmidt, Convective vortices and dust devils at the MSL landing site: Annual variability. *J. Geophys. Res.* **121**, 1514–1549 (2016).
18. D. Viúdez-Moreiras, J. Gómez-Elvira, C. E. Newman, S. Navarro, M. Marin, J. Torres, M. de la Torre-Juárez, Gale surface wind characterization based on the Mars Science Laboratory REMS dataset. Part I: Wind retrieval and Gale's wind speeds and directions. *Icarus* **319**, 909–925 (2019).
19. C. Charalambous, J. B. McClean, M. Baker, W. T. Pike, M. Golombek, M. Lemmon, V. Ansan, C. Perrin, A. Spiga, R. D. Lorenz, M. E. Banks, N. Murdoch, S. Rodriguez, C. M. Weitz, J. A. Grant, N. H. Warner, J. Garvin, I. J. Daubar, E. Hauber, A. E. Stott, C. L. Johnson, A. Mittelholz, T. Warren, S. Navarro, L. M. Sotomayor, J. Maki, A. Lucas, D. Banfield, C. Newman, D. Viúdez-Moreiras, J. Pla-García, P. Lognonné, W. B. Banerdt, Vortex-dominated aeolian activity at InSight's landing site, part 1: Multi-instrument observations, analysis and implications. *J. Geophys. Res.* **126**, e2020JE006757 (2021).
20. M. M. Baker, C. Newman, C. Charalambous, M. Golombek, A. Spiga, D. Banfield, M. Lemmon, M. Banks, R. Lorenz, J. Garvin, J. Grant, K. Lewis, V. Ansan, N. Warner, C. Weitz, S. Wilson, S. Rodriguez, Vortex-dominated aeolian activity at InSight's landing site, part 2: Local meteorology, transport dynamics, and model analysis. *J. Geophys. Res.* **121**, e2020JE006514 (2020).
21. J. A. Rodriguez-Manfredi, M. de la Torre Juárez, A. Alonso, V. Apéstigue, I. Arruego, T. Atienza, D. Banfield, J. Boland, M. A. Carrera, L. Castañer, J. Ceballos, H. Chen-Chen, A. Cobos, P. G. Conrad, E. Cordoba, T. del Río-Gaztelurrutia, A. de Vicente-Retortillo, M. Domínguez-Pumar, S. Espejo, A. G. Fairen, A. Fernández-Palma, R. Ferrándiz, F. Ferri, E. Fischer, A. García-Manchado, M. García-Villadangos, M. Genzer, S. Giménez, J. Gómez-Elvira, F. Gómez, S. D. Guzewich, A.-M. Harri, C. D. Hernández, M. Hieta, R. Hueso, I. Jaakonaho, J. J. Jiménez, V. Jiménez, A. Larman, R. Leiter, A. Lepinette, M. T. Lemmon, G. López, S. N. Madsen, T. Mäkinen, M. Marín, J. Martín-Soler, G. Martínez, A. Molina, L. Mora-Sotomayor, J. F. Moreno-Álvarez, S. Navarro, C. E. Newman, C. Ortega, M. C. Parrondo, V. Peinado, A. Peña, I. Pérez-Grande, S. Pérez-Hoyos, J. Pla-García, J. Polkko, M. Postigo, O. Prieto-Ballesteros, S. C. R. Rafkin, M. Ramos, M. I. Richardson, J. Romeral, C. Romero, K. D. Runyon, A. Saiz-Lopez, A. Sánchez-Lavega, I. Sard, J. T. Schofield, E. Sebastian, M. D. Smith, R. J. Sullivan, L. K. Tamppari, A. D. Thompson, D. Toledo, F. Torrero, J. Torres, R. Urquí, T. Velasco, D. Viúdez-Moreiras, S. Zurita; The MEDA Team, The Mars Environmental Dynamics Analyzer, MEDA. A suite of environmental sensors for the Mars 2020 mission. *Space Sci. Rev.* **217**, 48 (2021).
22. B. Chide, N. Murdoch, Y. Bury, S. Maurice, X. Jacob, J. P. Merrison, J. J. Iversen, P. Y. Meslin, M. Bassas-Portús, A. Cadu, A. Sournac, B. Dubois, R. D. Lorenz, D. Mimoun, R. C. Wiens, Experimental wind characterization with the SuperCam microphone under a simulated Martian atmosphere. *Icarus* **354**, 114060 (2021).
23. J. N. Maki, D. Gruel, C. McKinney, M. A. Ravine, M. Morales, D. Lee, R. Willson, D. Copley-Woods, M. Valvo, T. Goodsall, J. McGuire, R. G. Sellar, J. A. Schaffner, M. A. Caplinger, J. M. Shamah, A. E. Johnson, H. Ansari, K. Singh, T. Litwin, R. Deen, A. Culver, N. Ruoff, D. Petrizzo, D. Kessler, C. Basset, T. Estlin, F. Alibay, A. Nelessen, S. Algermissen, The Mars 2020 engineering cameras and microphone on the perseverance rover: A next-generation imaging system for mars exploration. *Space Sci. Rev.* **216**, 137 (2020).
24. J. F. Bell, J. N. Maki, G. L. Mehall, M. A. Ravine, M. A. Caplinger, Z. J. Bailey, S. Brylow, J. A. Schaffner, K. M. Kinch, M. B. Madsen, A. Winhold, A. G. Hayes, P. Corlies, C. Tate, M. Barrington, E. Cisneros, E. Jensen, K. Paris, K. Crawford, C. Rojas, L. Mehall, J. Joseph, J. B. Proton, N. Cluff, R. G. Deen, B. Betts, E. Cloutis, A. J. Coates, A. Colaprete, K. S. Edgett, B. L. Ehlmann, S. Fagents, J. P. Grotzinger, C. Hardgrove, K. E. Herkenhoff, B. Horgan, R. Jaumann, J. R. Johnson, M. Lemmon, G. Paar, M. Caballo-Perucha, S. Gupta, C. Traxler, F. Preusker, M. S. Rice, M. S. Robinson, N. Schmitz, R. Sullivan, M. J. Wolff, The Mars 2020 *Perseverance* Rover Mast Camera Zoom (Mastcam-Z) multispectral, stereoscopic imaging investigation. *Space Sci. Rev.* **217**, 24 (2021).
25. M. Chojnacki, M. Banks, A. Urso, Wind-driven erosion and exposure potential at Mars 2020 rover candidate-landing sites. *J. Geophys. Res.* **123**, 468–488 (2018).
26. M. Day, T. Dorn, Wind in Jezero crater, Mars. *Geophys. Res. Lett.* **46**, 3099–3107 (2019).
27. C. E. Newman, M. de la Torre Juárez, J. Pla-García, R. J. Wilson, S. R. Lewis, L. Neary, M. A. Kahre, F. Forget, A. Spiga, M. I. Richardson, F. Daerden, T. Bertrand, D. Viúdez-Moreiras, R. Sullivan, A. Sánchez-Lavega, B. Chide, J. A. Rodriguez-Manfredi, Multi-model meteorological and aeolian predictions for Mars 2020 and the Jezero crater region. *Space Sci. Rev.* **217**, 20 (2021).
28. J. Pla-García, S. C. R. Rafkin, G. M. Martinez, Á. Vicente-Retortillo, C. E. Newman, H. Savijärvi, M. de la Torre, J. A. Rodriguez-Manfredi, F. Gómez, A. Molina, D. Viúdez-Moreiras, A. M. Harri, Meteorological predictions for *Mars 2020 Perseverance Rover* landing site at Jezero crater. *Space Sci Rev.* **216**, 148 (2020).
29. M. I. Richardson, A. D. Toigo, C. E. Newman, PlanetWRF: A general purpose, local to global numerical model for planetary atmospheric and climate dynamics. *J. Geophys. Res.* **112**, E09001 (2007).
30. R. W. Zurek, C. B. Leovy, Thermal tides in the dusty martian atmosphere: A verification of theory. *Science* **213**, 4506, 437–439 (1981).
31. R. J. Wilson, K. P. Hamilton, Comprehensive model simulation of thermal tides in the martian atmosphere. *J. Atmos. Sci.* **53**, 1290–1326 (1996).
32. D. Viúdez-Moreiras, C. E. Newman, F. Forget, M. Lemmon, D. Banfield, A. Spiga, A. Lepinette, J. A. Rodriguez-Manfredi, J. Gómez-Elvira, J. Pla-García, N. Muller, M. Grott, Effects of a large dust storm in the near-surface atmosphere as measured by InSight in Elysium Planitia, Mars. Comparison with contemporaneous measurements by Mars Science Laboratory. *J. Geophys. Res.* **125**, e2020JE006493 (2020).
33. S. Morgan, R. Raspet, Investigation of the mechanisms of low-frequency wind noise generation outdoors. *J. Acoust. Soc. Am.* **92**, 1180–1183 (1992).
34. A. Spiga, N. Murdoch, R. Lorenz, F. Forget, C. Newman, S. Rodriguez, J. Pla-Garcia, D. V. Moreiras, D. Banfield, C. Perrin, N. T. Mueller, M. Lemmon, E. Millour, W. B. Banerdt, A study of daytime convective vortices and turbulence in the Martian planetary boundary layer based on half-a-year of InSight atmospheric measurements and large-eddy simulations. *J. Geophys. Res.* **126**, e2020JE006511 (2021).
35. R. D. Lorenz, M. T. Lemmon, J. Maki, First Mars year of observations with the InSight solar arrays: Winds, dust devil shadows, and dust accumulation. *Icarus* **364**, 114468 (2021).
36. A. Spiga, Comment on "'Observing desert dust devils with a pressure logger" by Lorenz (2012)—Insights on measured pressure fluctuations from large-eddy simulations. *Geosci. Instrum. Method. Data Syst.* **1**, 151–154 (2012).
37. T. I. Michaels, S. C. R. Rafkin, Large-eddy simulation of atmospheric convection on Mars. *Q. J. Roy. Meteorol. Soc.* **130**, 1251–1274 (2004).
38. T. I. Michaels, S. C. R. Rafkin, Meteorological predictions for candidate 2007 Phoenix Mars Lander sites using the Mars Regional Atmospheric Modeling System (MRAMS). *J. Geophys. Res.* **113**, E12 (2008).

39. G. Willis, J. Deardorff, Laboratory observations of turbulent penetrative–convection planforms. *J. Geophys. Res.* **84**, 295–302 (1979).
40. Z. Wu, M. I. Richardson, X. Zhang, J. Cui, N. G. Heavens, C. Lee, T. Li, Y. Lian, C. E. Newman, A. Soto, O. Temel, A. D. Toigo, M. Witek, Large Eddy Simulations of the dusty Martian convective boundary layer with MarsWRF. *J. Geophys. Res.* **126**, e2020JE006752 (2021).
41. R. Sullivan, R. Greeley, M. Kraft, G. Wilson, M. Golombek, K. Herkenhoff, J. Murphy, P. Smith, Results of the Imager for Mars Pathfinder windsock experiment. *J. Geophys. Res.* **105**, 24547–24562 (1998).
42. M. Klose, Y. Shao, Large-eddy simulation of turbulent dust emission. *Aeolian Res.* **8**, 49–58 (2013).
43. Y. Shao, W. Nickling, G. Bergametti, H. Butler, A. Chappell, P. Findlater, J. Gillies, M. Ishizuka, M. Klose, J. F. Kok, J. Leys, H. Lu, B. Marticorena, G. McTainsh, G. McKenna-Neuman, G. S. Okin, C. Strong, N. Webb, A tribute to Michael R. Raupach for contributions to aeolian fluid dynamics. *Aeolian Res.* **19**, 37–54 (2015).
44. N. O. Renno, V. J. Abreu, J. Koch, P. H. Smith, O. K. Hartogensis, H. A. R. De Bruin, D. Burose, G. T. Delory, W. M. Farrell, C. J. Watts, J. Garatuza, M. Parker, A. Carswell, MATADOR 2002: A pilot field experiment on convective plumes and dust devils. *J. Geophys. Res.* **109**, E07001 (2004).
45. S. C. R. Rafkin, B. Jemmett-Smith, L. Fenton, R. Lorenx, T. Takemi, J. Ito, D. Tyler, Dust devil formation. *Space Sci. Rev.* **203**, 183–207 (2016).
46. Y. Z. Zhao, Z. L. Gu, Y. Z. Yu, Y. Ge, Y. Li, X. Feng, Mechanism and large eddy simulation of dust devils. *Atmosp. Ocean* **42**, 61–84 (2004).
47. I. Ordóñez-Etxeberria, R. Hueso, A. Sánchez-Lavega, A systematic search of sudden pressure drops on Gale crater during two Martian years derived from MSL/REMS data. *Icarus* **299**, 308–330 (2018).
48. B. Jackson, Vortices and dust devils as observed by the Mars Environmental Dynamics Analyzer instruments on board the Mars 2020 Perseverance rover. *Plan. Sci. J.* **3**, 20 (2022).
49. N. O. Renno, M. L. Burkett, M. P. Larkin, A simple thermodynamical theory for dust devils. *J. Atmos. Sci.* **55**, 3244–3252 (1998).
50. M. V. Kurgansky, R. D. Lorenz, N. O. Renno, T. Takemi, Z. Gu, W. Wei, Dust devil steady-state structure from a fluid dynamics perspective. *Space Sci Rev* **203**, 209–244 (2016).
51. I. Ordóñez-Etxeberria, R. Hueso, A. Sánchez-Lavega, Strong increase in dust devil activity at Gale crater on the third year of the MSL mission and suppression during the 2018 Global Dust Storm. *Icarus* **347**, 113814 (2020).
52. M. D. Ellehoj, H. P. Gunnlaugsson, P. A. Taylor, H. Kahanpää, K. M. Bean, B. A. Cantor, B. T. Gheynani, L. Drube, D. Fisher, A.-M. Harri, C. Holstein-Rathlou, M. T. Lemmon, M. B. Madsen, M. C. Malin, J. Polkko, P. H. Smith, L. K. Tamppari, W. Wen, J. Whiteway, Convective vortices and dust devils at the Phoenix Mars mission landing site. *J. Geophys. Res.* **115**, E00E16 (2010).
53. R. D. Lorenz, A. Spiga, P. Lognonné, M. Plasman, C. E. Newman, C. Charalambous, The whirlwinds of Elysium: A catalog and meteorological characteristics of "dust devil" vortices observed by InSight on Mars. *Icarus* **355**, 114119 (2021).
54. M. Golombek, D. Kass, N. Williams, N. Warner, I. Daubar, S. Piqueux, C. Charalambous, W. T. Pike, Assessment of InSight landing site predictions. *J. Geophys. Res.* **125**, e2020JE006502 (2020).
55. G. M. Martínez, A. Vicente-Retortillo, A. R. Vasavada, C. E. Newman, E. Fischer, N. O. Rennó, H. Savijärvi, M. de la Torre, I. Ordóñez-Etxeberria, M. T. Lemmon, S. D. Guzewich, T. H. McConnochie, E. Sebastián, R. Hueso, A. Sánchez-Lavega, The surface energy budget at Gale crater during the first 2500 sols of the Mars Science Laboratory mission. *J. Geophys. Res.* **126**, e2020JE006804 (2021).
56. R. L. Fergason, P. R. Christensen, M. P. Golombek, T. J. Parker, Surface properties of the Mars science laboratory candidate landing sites: Characterization from orbit and predictions. *Space Sci. Rev.* **170**, 739–773 (2012).
57. R. D. Lorenz, G. M. Martínez, A. Spiga, A. Vicente-Retortillo, C. E. Newman, N. Murdoch, F. Forget, E. Millour, T. Pierron, Lander and rover histories of dust accumulation on and removal from solar arrays on Mars. *Plan. Space Sci.* **207**, 105337 (2021).
58. D. Banfield, A. Spiga, C. Newman, F. Forget, M. Lemmon, R. Lorenz, N. Murdoch, D. Viudez-Moreiras, J. Pla-Garcia, R. F. Garcia, P. Lognonné, Ö. Karatekin, C. Perrin, L. Martire, N. Teanby, B. V. Hove, J. N. Maki, B. Kenda, N. T. Mueller, S. Rodriguez, T. Kawamura, J. B. McClean, A. E. Stott, C. Charalambous, E. Millour, C. L. Johnson, A. Mittelholz, A. Määttänen, S. R. Lewis, J. Clinton, S. C. Stähler, S. Ceylan, D. Giardini, T. Warren, W. T. Pike, I. Daubar, M. Golombek, L. Rolland, R. Widmer-Schnidrig, D. Mimoun, É. Beucler, A. Jacob, A. Lucas, M. Baker, V. Ansan, K. Hurst, L. Mora-Sotomayor, S. Navarro, J. Torres, A. Lepinette, A. Molina, M. Marin-Jimenez, J. Gomez-Elvira, V. Peinado, J. A. Rodriguez-Manfredi, B. T. Carcich, S. Sackett, C. T. Russell, T. Spohn, S. E. Smrekar, W. B. Banerdt, The atmosphere of Mars as observed by InSight. *Nat. Geo.* **13**, 190–198 (2020).
59. A. Spiga, E. Barth, Z. Gu, F. Hoffmann, J. Ito, B. Jemmett-Smith, M. Klose, S. Nishizawa, S. Raasch, S. Rafkin, T. Takemi, D. Tyler, W. Wei, Large-eddy simulations of dust devils and convective vortices. *Space Sci. Rev.* **203**, 245–275 (2016).
60. G. M. Martínez, C. N. Newman, A. de Vicente-Retortillo, E. Fischer, N. O. Renno, M. I. Richardson, A. G. Fairén, M. Genzer, S. D. Guzewich, R. M. Haberle, A. M. Harri, O. Kemppinen, M. T. Lemmon, M. D. Smith, M. de la Torre-Juárez, A. R. Vasavada, The modern near-surface martian climate: A review of in-situ meteorological data from viking to curiosity. *Space Sci. Rev.* **212**, 295–338 (2017).
61. N. T. Bridges, R. Sullivan, C. E. Newman, S. Navarro, J. van Beek, R. C. Ewing, F. Ayoub, S. Silvestro, O. Gasnault, S. Le Mouélic, M. G. A. Lapotre, W. Rapin, Martian aeolian activity at the Bagnold Dunes, Gale Crater: The view from the surface and orbit. *J. Geophys. Res. Plan.* **122**, 2077–2110 (2017).
62. D. Viúdez-Moreiras, J. Gómez-Elvira, C. E. Newman, S. Navarro, M. Marin, J. Torres, M. de la Torre-Juárez, Gale surface wind characterization based on the Mars Science Laboratory REMS dataset. Part II: Wind probability distributions. *Icarus* **319**, 645–656 (2019).
63. P. A. Taylor, D. C. Catling, M. Daly, C. S. Dickinson, H. P. Gunnlaugsson, A.-M. Harri, C. F. Lange, Temperature, pressure and wind instrumentation on the Phoenix meteorological package. *J. Geophys. Res.* **113**, EA0A10 (2008).
64. A.-M. Harri, M. Genzer, O. Kemppinen, H. Kahanpää, J. Gomez-Elvira, J. A. Rodriguez-Manfredi, R. Haberle, J. Polkko, W. Schmidt, H. Savijärvi, J. Kauhanen, E. Atlaskin, M. Richardson, T. Siili, M. Paton, M. de la Torre Juarez, C. Newman, S. Rafkin, M. T. Lemmon, M. Mischna, S. Merikallio, H. Haukka, J. Martin-Torres, M.-P. Zorzano, V. Peinado, R. Urqui, A. Lapinette, A. Scodary, T. Mäkinen, L. Vazquez, N. Rennó; the REMS/MSL Science Team, Pressure observations by the Curiosity rover: Initial results. *J. Geophys. Res. Planets* **119**, 2132–2147 (2014).
65. M. Domínguez, V. Jimenez, J. Ricart, L. Kowalski, J. Torres, S. Navarro, J. Romeral, L. Castener, A hot film anemometer for the Martian atmosphere. *Planet. Space Sci.* **56**, 1169–1179 (2008).
66. J. Perez-Izquierdo, E. Sebastián, G. M. Martínez, A. Bravo, M. Ramos, J. A. Rodríguez Manfredi, The Thermal Infrared Sensor (TIRS) of the Mars Environmental Dynamics Analyzer (MEDA) instrument onboard Mars 2020, a general description and performance analysis. *Measurement* **122**, 432–442 (2018).
67. A. Graf, M. Arndt, M. Sauer, G. Gerlach, Review of micromachined thermopiles for infrared detection. *Meas. Sci. Technol.* **18**, R59 (2007).
68. E. Sebastián, G. Martínez, M. Ramos, F. Haenschke, R. Ferrándiz, M. Fernández, J. A. Rodríguez Manfredi, Radiometric and angular calibration tests for the MEDA-TIRS radiometer onboard NASA's Mars 2020 mission. *Measurement* **164**, 107968 (2020).
69. E. Sebastián, G. Martínez, M. Ramos, I. Pérez-Grande, J. Sobrado, J. A. Rodríguez Manfredi, Thermal calibration of the MEDA-TIRS radiometer onboard NASA's Perseverance rover. *Acta Astronaut.* **182**, 144–159 (2021).
70. V. Apestigue, A. Gonzalo, J. J. Jiménez, J. Boland, M. Lemmon, J. R. de Mingo, E. García-Menendez, J. Rivas, J. Azcue, L. Bastide, N. Andrés-Santiuste, J. Martínez-Oter, M. González-Guerrero, A. Martin-Ortega, D. Toledo, F. J. Alvarez-Rios, F. Serrano, B. Martín-Vodopivec, J. Manzano, R. López Heredero, I. Carrasco, A. Aparicio, A. Carretero, D. R. MacDonald, L. B. Moore, M. Á. Alcacera, J. A. Fernández-Viguri, I. Martín, M. Yela, M. Álvarez, P. Manzano, J. A. Martín, J. C. del Hoyo, M. Reina, R. Urqui, J. A. Rodriguez-Manfredi, M. de la Torre Juárez, C. Hernandez, E. Cordoba, R. Leiter, A. Thompson, S. Madsen, M. D. Smith, D. Viúdez-Moreiras, A. Saiz-Lopez, A. Sánchez-Lavega, L. Gomez-Martín, G. M. Martínez, F. J. Gómez-Elvira, I. Arruego, Radiation and Dust Sensor for Mars Environmental Dynamic Analyzer Onboard M2020 Rover. *Sensors* **22**, 2907 (2022).
71. S. Maurice, R. C. Wiens, P. Bernardi, P. Caïs, S. Robinson, T. Nelson, O. Gasnault, J. M. Reess, M. Deleuze, F. Rull, J. A. Manrique, S. Abbaki, R. B. Anderson, Y. André, S. M. Angel, G. Arana, T. Battault, P. Beck, K. Benzerara, S. Bernard, J. P. Berthias, O. Beyssac, M. Bonafous, B. Bousquet, M. Boutillier, A. Cadu, K. Castro, F. Chapron, B. Chide, K. Clark, E. Clavé, S. Clegg, E. Cloutis, C. Collin, E. C. Cordoba, A. Cousin, J. C. Dameury, W. D'Anna, Y. Daydou, A. Debus, L. Deflores, E. Dehouck, D. Delapp, G. de Los Santos, C. Donny, A. Doressoundiram, G. Dromart, B. Dubois, A. Dufour, M. Dupieux, M. Egan, J. Ervin, C. Fabre, A. Fau, W. Fischer, O. Forni, T. Fouchet, J. Frydenvang, S. Gauffre, M. Gauthier, V. Gharakanian, O. Gilard, I. Gontijo, R. Gonzalez, D. Granena, J. Grotzinger, R. Hassen-Khodja, M. Heim, Y. Hello, G. Hervet, O. Humeau, X. Jacob, S. Jacquinod, J. R. Johnson, D. Kouach, G. Lacombe, N. Lanza, L. Lapauw, J. Laserna, J. Lasue, L. le Deit, S. le Mouélic, E. le Comte, Q. M. Lee, C. Legett IV, R. Leveille, E. Lewin, C. Leyrat, G. Lopez-Reyes, R. Lorenz, B. Lucero, J. M. Madariaga, S. Madsen, M. Madsen, N. Mangold, F. Manni, J. F. Mariscal, J. Martinez-Frias, K. Mathieu, R. Mathon, K. P. McCabe, T. McConnochie, S. M. McLennan, J. Mekki, N. Melikechi, P. Y. Meslin, Y. Micheau, Y. Michel, J. M. Michel, D. Mimoun, A. Misra, G. Montagnac, C. Montaron, F. Montmessin, J. Moros, V. Mousset, Y. Morizet, N. Murdoch, R. T. Newell, H. Newsom, N. Nguyen Tuong, A. M. Ollila, G. Orttner, L. Oudda, L. Pares, J. Parisot, Y. Parot, R. Pérez, D. Pheav, L. Picot, P. Pilleri, C. Pilorget, P. Pinet, G. Pont, F. Poulet, C. Quantin-Nataf, B. Quertier, D. Rambaud, W. Rapin, P. Romano, L. Roucayrol, C. Royer, M. Ruellan, B. F. Sandoval, V. Sautter, M. J. Schoppers, S. Schröder, H. C. Seran, S. K. Sharma, P. Sobron, M. Sodki, A. Sournac, V. Sridhar, D. Standarovsky, S. Storms, N. Striebig, M. Tatat, M. Toplis, I. Torre-Fdez, N. Toulemont, C. Velasco, M. Veneranda, D. Venhaus, C. Virmontois, M. Viso, P. Willis, K. W. Wong, The

SuperCam Instrument Suite on the Mars 2020 Rover: Science objectives and mast-unit description. *Space Sci. Rev.* **217**, 47 (2021).
72. K. Lettau, H. H. Lettau, Experimental and micro-meteorological field studies of dune migration, in *Exploring the World's Driest Climate*, H. H. Lettau, K. Lettau, Eds. (IES Report 101, University of Wisconsin-Madison, 1978), pp. 110–147.
73. A. D. Toigo, C. Lee, C. E. Newman, M. I. Richardson, The impact of resolution on the dynamics of the martian global atmosphere: Varying resolution studies with the MarsWRF GCM. *Icarus* **221**, 276–288 (2012).
74. C. E. Newman, J. Gómez-Elvira, M. Marin, S. Navarro, J. Torres, M. I. Richardson, J. M. Battalio, S. D. Guzewich, R. Sullivan, M. Torre, A. R. Vasavada, N. T. Bridges, Winds measured by the Rover Environmental Monitoring Station (REMS) during the Mars Science Laboratory (MSL) rover's Bagnold Dunes Campaign and comparison with numerical modeling using MarsWRF. *Icarus* **291**, 203–231 (2017).
75. C. E. Newman, H. Kahanpää, M. I. Richardson, G. M. Martínez, A. Vicente-Retortillo, M. T. Lemmon, MarsWRF Convective vortex and dust devil predictions for Gale crater over 3 mars years and comparison with MSL-REMS observations. *J. Geophys. Res.* **124**, 3442–3468 (2019).
76. M. A. Mischna, C. Lee, M. I. Richardson, Development of a fast, accurate radiative transfer model for the Martian atmosphere, past and present. *J. Geophys. Res.* **117**, E10009 (2012).
77. C. Lee, M. I. Richardson, C. E. Newman, M. A. Mischna, The sensitivity of solsticial pauses to atmospheric ice and dust in the MarsWRF General Circulation Model. *Icarus* **311**, 23–34 (2018).
78. S.-Y. Hong, H.-L. Pan, Nonlocal boundary layer vertical diffusion in a medium-range forecast model. *Mon. Wea. Rev.* **124**, 2322–2339 (1996).
79. J. E. Laity, N. T. Bridges, Ventifacts on Earth and Mars: Analytical, field, and laboratory studies supporting sand abrasion and windward feature development. *Geomorphology* **105**, 202–217 (2009).

Acknowledgments: We gratefully acknowledge the effort by the huge entire Mars 2020 team to meet our launch date despite the COVID-19 pandemic, to land and deploy instruments successfully in Jezero crater, and to conduct operations on the surface of Mars since February 2021. This paper arose from discussions within the Mars 2020 Atmospheres Working Group but would not have been possible without the tremendous contributions of everyone involved in Mars 2020 operations. We wish to especially pay tribute to the many team members based in Europe who regularly work through the night as MEDA or SuperCam Payload Uplink and Downlink Leads (PULs/PDLs) or in other roles and to all those who had shifts as Atmospheres Working Group representatives during this period. Last, we gratefully acknowledge the very helpful and constructive comments from both anonymous reviewers. **Funding:** R.H., A.S.-L., A.M., and T.d.R.-G. are supported by Spanish Ministry of Science and Innovation project PID2019-109467GB-I00 funded by MCIN/AEI/10.13039/501100011033/ and Grupos Gobierno Vasco IT1366-19. I.A., D.T., and V.A. are supported by the Spanish National Research, Development, and Innovation Program through the grants RTI2018-099825-B-C31, ESP2016-80320-C2-1-R, and ESP2014-54256-C4-3-R. L.M., S.N., and J.G.-E. are supported by the Spanish Ministry of Economy and Competitiveness, projects ESP2014-54256-C4-1-R and AYA2015-65041-P; the Spanish Ministry of Science, Innovation, and Universities, projects ESP2016-79612-C3-1-R, ESP2016-80320-C2-1-R, RTI2018-098728-B-C31, and RTI2018-099825-B-C31; and the Spanish Ministry of Science and Innovation's Centre for the Development of Industrial Technology, projects RTI2018-098728-B-C31 and RTI2018-099825-B-C31. Á.V.-R. and M.-P.Z. are supported by Spanish State Research Agency (AEI) project no. MDM-2017-0737 Unidad de Excelencia "María de Maeztu"–Centro de Astrobiología (INTA-CSIC). M.-P.Z. is supported by the Spanish Ministry of Science and Innovation, PID2019-104205GB-C21. M.M.B. and M.-P.Z. are supported by NASA's Mars 2020 Participating Scientist Program. All other authors were supported by funding from the Mars 2020 mission, part of the NASA Mars Exploration Program. Work by C.E.N. was additionally funded by the InSight Participating Scientist Program. A portion of this work was performed at the Jet Propulsion Laboratory, California Institute of Technology, under a contract with NASA and funding by SMD, GCD, and STMD. **Author contributions:** Conceptualization: All authors. Data curation: S.N., J.G.-E., E.S., L.M., A.L., C.E.N., M.I.R., R.H., D.T., V.A., I.A., R.S., and K.E.H. Formal analysis: R.H., M.T.L., C.E.N., A.M., Á.V.-R., V.A., G.M.M., D.T., R.S., K.E.H., M.d.l.T.J., D.V.-M., and J.N.M. Investigation: M.J.W., M.T.L., M.d.l.T.J., C.E.N., R.H., J.A.R.M., L.T., T.H.M., C.T., G.M.M., D.T., E.F., R.S., D.M., A.E.S., N.M., F.G., P.P., T.d.R.-G., D.V.-M., P.C., S.N., J.F.B., J.N.M., R.C.W., B.Ch., M.-P.Z., L.M., M.M.B., D.B., J.P.-G., A.L., and R.F. Methodology: M.T.L., R.H., C.E.N., M.I.R., A.M., Á.V.-R., V.A., G.M.M., D.T., R.S., K.E.H., M.d.l.T.J., A.E.S., N.M., I.A., S.M., J.G.-E., and D.M. Project administration/supervision: C.E.N., M.J.W., M.T.L., M.d.l.T.J., J.A.R.M., J.F.B., J.N.M., R.C.W., and I.A. Resources: M.d.l.T.J., J.F.B., J.N.M., J.A.R.M., R.C.W., and S.M. Visualization: R.H., M.T.L., C.E.N., Á.V.-R., M.I.R., A.E.S., and N.M. Writing—Original draft: C.E.N., R.H., and M.T.L. Writing—Review and editing: C.E.N., R.H., M.T.L., A.M., A.E.S., R.S., G.M.M., K.E.H., A.S.-L., M.d.l.T.J., N.M., L.T., D.V.-M., D.T., V.A., T.B., A.B., B. Clark, O.B., R.D.L., P.C., and F.G. **Competing interests:** The authors declare that they have no competing interests. **Data and materials availability:** All Mars 2020 MEDA data used in this paper are available via the Planetary Data System (PDS) Atmospheres node at https://doi.org/10.17189/1522849. All InSight APSS data used were already available in the PDS at https://doi.org/10.17189/1518939. Mars 2020 SuperCam microphone recordings are available via the PDS at https://doi.org/10.17189/1522646. Calibrated image products from Mars 2020 Mastcam-Z and Navcam are available at https://doi.org/10.17189/q3ts-c749 and https://doi.org/10.17189/yvkm-rx37, respectively. A list of vortex pressure drops detected in Mars 2020 MEDA and InSight APSS data, a list of RDS dust event detections, and the measurements of wind tails and ventifacts orientations shown in Fig. 2B are provided in the Supplementary Materials. Output from the MarsWRF mesoscale simulation and LES shown in this paper are archived at https://doi.org/10.5281/zenodo.6412722.

Submitted 22 November 2021
Accepted 8 April 2022
Published 25 May 2022
10.1126/sciadv.abn3783